Experimental Thermal and Fluid Science 175 (2026) 111743

Contents lists available at ScienceDirect

Experimental Thermal and Fluid Science

journal homepage: www.elsevier.com/locate/etfs

Impact of wall-heating on the development of crossflow instability

Marina Barahona [a,*], Yifu Chen [a], Alberto F. Rius-Vidales [b], Marios Kotsonis [a]

[a] Flow Physics and Technology, Faculty of Aerospace Engineering, Delft University of Technology, 2629HS, Delft, The Netherlands
[b] Maritime and Transport Technology, Faculty of Mechanical Engineering, Delft University of Technology, 2628CD, Delft, The Netherlands

ARTICLE INFO

Keywords:
Wall-heating
Crossflow instability
Laminar-to-turbulent transition
Secondary instabilities

ABSTRACT

Efficient thermal management is critical for future electric aircraft. An innovative approach (Outer Mold Line cooling) leverages the aircraft's aerodynamic surfaces for heat dissipation, heating the adjacent boundary layer. It is known that wall-heating can have detrimental effects on laminar–turbulent transition driven by stationary crossflow instabilities (S-CFI). However, its impact remains largely unclear due to a lack of experimental studies. This work investigates the effect of a heated wall across all stages of S-CFI development, spanning linear growth, non-linear saturation, and laminar-turbulent transition. This is achieved through comprehensive wind-tunnel experiments, complemented by comparisons with Compressible Nonlinear Parabolized Stability Equations (CNPSE) results. Results show that wall-heating increases the boundary-layer momentum deficit and the crossflow velocity component, leading to increased destabilization of S-CFI. In turn, higher S-CFI amplitudes promote an earlier onset of non-linear interactions between stationary, traveling, and secondary instability modes. Notably, under equivalent freestream turbulence (T_u) levels, wall-heating results in a higher S-CFI saturation amplitude compared to adiabatic conditions. In addition, spectral analysis reveals substantial amplification of unsteady perturbations with wall-heating. A key finding of this work is the strong destabilization of traveling CFI under wall-heating, which persists into the nonlinear regime and yields highly amplified type-III instabilities. One possible implication of the strong destabilization of T-CFI and type-III instabilities is that at sufficiently high wall-to-freestream temperature ratios, T-CFI could dominate the transition process, potentially leading to a transition scenario similar to that observed under high levels of freestream turbulence.

1. Introduction

Effective thermal management of batteries and fuel cells remains a critical technological challenge in the electrification of future aircraft. Unlike conventional turbofan engines, where the heat generated is mainly rejected naturally through the engine gas exhaust, electric-based propulsion systems rely solely on conduction for heat dissipation [1]. To ensure efficient operation, the heat generated by the fuel cell must be removed by an active cooling system. For a 150-passenger aircraft (e.g., Airbus A319), the total power requirement can reach 22 MW during take-off [2]. If the aircraft is equipped with Proton Exchange Membrane Fuel Cells (PEMFC), assuming a nominal fuel-cell efficiency of approximately 50% [3], the fuel-cell cooling system of the electrified Airbus A319 would need to dissipate approximately 11 MW of heat during take-off. Given these high thermal loads, dedicated onboard thermal management systems are essential to prevent thermal buildup and ensure reliable operation.

A promising approach to this challenging demand for heat dissipation involves leveraging the aircraft's aerodynamic surfaces, thereby minimizing or eliminating the need for traditional thermal management solutions, such as ram-air heat exchangers. These conventional systems often demand additional volume and weight, imposing design constraints and increasing aerodynamic drag. In contrast, dissipating heat through the aircraft's external skin, an approach known as Outer Mold Line (OML) cooling, requires fewer components and avoids modifications to the aerodynamic surfaces, reducing weight and drag [4].

The leading edge (LE) of an aircraft constitutes one of the most effective areas for heat dissipation [4]. The rapid acceleration experienced by the boundary-layer flow near the LE enhances convective heat transfer between the aircraft skin and the surrounding air. Unfortunately, the presence of a heated surface can potentially destabilize the laminar boundary-layer developing at the LE, leading to a premature onset of laminar-to-turbulent transition, thereby increasing skin friction drag and reducing the overall aerodynamic efficiency.

Recent studies (e.g., [1,5]) have investigated the impact of OML cooling using RANS computations, providing valuable insights on the

* Corresponding author.
E-mail address: M.BarahonaLopez@tudelft.nl (M. Barahona).

https://doi.org/10.1016/j.expthermflusci.2026.111743
Received 5 December 2025; Received in revised form 22 March 2026; Accepted 31 March 2026
Available online 2 April 2026

overall aerodynamic performance. However, to accurately quantify the impact of thermal effects on skin friction drag in transitional flows, high-fidelity simulations like Direct Numerical Simulations (DNS) coupled with wind tunnel experiments are required. Unfortunately, research employing these methodologies remains limited, making accurate drag penalty predictions for OML cooling systems particularly challenging.

In gas flow boundary layers, the presence of a solid wall at a relatively higher temperature than the ambient flow increases the fluid's near-wall viscosity, leading to a decrease of momentum in the near-wall region. In turn, modifications in the velocity field affect the growth of disturbances within the boundary layer and eventually the onset of laminar-to-turbulent transition. Considering a contemporary airliner, when a wing features low sweep ($\Lambda \leq 25°$), laminar-to-turbulent transition is primarily governed by Tollmien–Schlichting (TS) waves, while crossflow instabilities (CFI) dominate the transition process in wings with sweep angles greater than 35° [6]. Due to the different growth behavior and nature of these two types of instabilities, findings regarding the impact of non-adiabatic walls on TS wave development differ from CFI (both traveling, T-CFI, and stationary, S-CFI).

It has been previously demonstrated through experiments (e.g., [7,8]) and linear stability theory (e.g., [9,10]) that TS waves are significantly stabilized in the presence of cooled walls, and destabilized with heated walls. The experimental results from Kachanov et al. [7] showed that even a mild cooling temperature ratio of $T_w/T_e = 0.945$[1] resulted into a critical Reynolds number ($\mathrm{Re}_{\mathrm{crit}}$) two times higher than the $\mathrm{Re}_{\mathrm{crit}}$ in adiabatic conditions.

Contrary to TS waves, the effectiveness of thermal flow control towards (de)stabilizing CFI remains a point of debate. Linear Stability Theory (LST) analyses presented in [11–13] indicate that, similar to TS waves, S-CFI are stabilized by uniform wall-cooling and destabilized by uniform wall-heating. However, unlike TS waves, the findings of Lekoudis [12] suggest that the stabilizing effect of wall cooling on S-CFI is significantly weaker. A similar behavior was observed by Bertolotti and Bieler [14] using Compressible Linear Parabolized Stability Equations (CLPSE), and by Lemarechal et al. [15] in experiments on a swept wing. In Lemarechal et al. [15], a large section of a 25-degree swept wing was heated with a mild temperature ratio of $T_w/T_\infty = 1.04$, presenting no significant shift in the transition front. Combined, the available literature suggests that S-CFI exhibits minimal or no sensitivity to changes in wall temperature.

Saric and Reed [16] attributed the different thermal sensitivity between TS waves and S-CFI to the different nature of their instability mechanisms. More specifically, since TS waves are primarily driven by viscosity, their growth is more susceptible to near-wall viscosity modifications, whereas S-CFI, governed by an inviscid inflectional instability, exhibit a weaker dependence on thermal effects and a higher dependence on the velocity profile shape of the steady laminar baseflow [16]. However, the absence of a detailed mathematical formalism or experimental evidence to support this hypothesis challenges its validity.

Experimental conclusions regarding the effect of non-adiabatic walls on S-CFI often remain ambiguous due to the simultaneous presence of both traveling and stationary CFI. For freestream turbulence intensities (T_u) above 0.2%, T-CFI become the dominant instability [17]. However, the specific T_u threshold required to achieve a purely S-CFI-dominated transition scenario is still unclear, as turbulence intensity metrics employed across different experiments differ [18]. One clear example is the work of Eppink and Wlezien [19], where in spite of reporting low turbulence intensity values ($T_u = 0.02\%$), T-CFI reached significant amplitude levels. Interestingly, in the experiments of Eppink and Wlezien [19], when mild uniform cooling conditions ($T_w/T_\infty \approx 0.97$) were applied on a 35-degree swept wing, T-CFI exhibited stronger stabilization compared to S-CFI. This finding is further supported by the linear stability analysis of Ren and Kloker [13], which confirms the higher sensitivity of T-CFI to non-adiabatic wall conditions compared to S-CFI. In summary, the aforementioned studies highlight the sensitivity of T-CFI to changes in the wall temperature. The latter challenges the explanation proposed by Saric and Reed [16], which attributes the different thermal sensitivities of TS waves and CFI to their distinct instability mechanisms. Notably, traveling CFI are also inflectional, yet they remain significantly affected by thermal effects, as reported in Eppink and Wlezien [19] and Ren and Kloker [13].

Collectively, these observations highlight a largely ambiguous understanding of the impact of non-adiabatic conditions on crossflow-dominated transition. This ambiguity can be largely attributed to the lack of: (i) dedicated and systematic experimental investigations and (ii) non-linear numerical simulations investigating the effect of non-adiabatic walls across all different stages of S-CFI development, encompassing both linear and non-linear development. As a result, it remains difficult to demonstrate whether S-CFI remain insensitive to near-wall temperature changes.

Motivated by this gap, this study investigates the impact of a heated wall across all stages of S-CFI development, spanning linear growth, nonlinear saturation, and laminar-turbulent transition. This is achieved through comprehensive wind-tunnel experiments, complemented by comparisons with Compressible Nonlinear Parabolized Stability Equations (CNPSE) results. Hot-Wire Anemometry (HWA) and Cold-Wire Anemometry (CWA) are employed to measure both velocity and thermal boundary layers, respectively, along planes normal to the wall and parallel to the leading edge of a swept flat plate geometry at different streamwise locations. These measurements provide valuable insight into the signature of the perturbation in both the temporal and spatial domains, enabling the study of primary and secondary CFI. In particular, the focus will be placed on comparing the perturbation evolution under adiabatic and wall-heating conditions. To the best of the authors' knowledge, this work presents the first comparison between experimental measurements and CNPSE results under non-adiabatic wall conditions, providing new insights into how wall-heating affects the nonlinear growth regime of S-CFI.

2. Methodology

2.1. Experimental setup and flow measurement techniques

Experiments are performed in the A-tunnel, a low-turbulence, open-jet, subsonic, and anechoic wind tunnel located at the Delft University of Technology [20]. A cross-sectional view of the wind tunnel facility is illustrated in Fig. 1(a). The flow is driven by two 30 kW centrifugal fans to the settling chamber, where it encounters a straightener and four anti-turbulence screens. Thereafter the flow is accelerated through a 17:1 cylindrical contraction until it reaches the test chamber. A nozzle adapts the circular inlet at the plenum of diameter 600 mm to the rectangular test section with dimensions 250 × 1000 mm^2 on top of which the swept flat plate setup is placed.

The freestream velocity measured at the nozzle outlet is $U_\infty = \sqrt{2q_\infty/\rho_\infty} = 15.73$ m/s, where the dynamic pressure is computed from the difference[2] between the total and static pressure measured at a Pitot-static tube located 500 mm upstream of the LE. The chord-based Reynolds number is $\mathrm{Re}_{c_X} = U_\infty c_X/\nu_\infty = 8.56 \times 10^5$, where c_X is the chord parallel to the X-coordinate (see Fig. 1b), and specified in Table 1. The freestream air density (ρ_∞) and kinematic viscosity (ν_∞) are obtained from the freestream ambient temperature (T_∞) and pressure (P_∞), measured at the test chamber by means of a Resis-

[1] Throughout the present work temperature ratios are expressed using temperatures in Kelvin scale. Thus, T_w/T_e is composed of T_w, the wall temperature, and T_e, the flow external temperature (i.e., outside of the boundary layer).

[2] Differential pressure sensor by Honeywell (sps.honeywell.com), model: RSC-005ND, range ±1246 Pa, accuracy ±13 Pa.

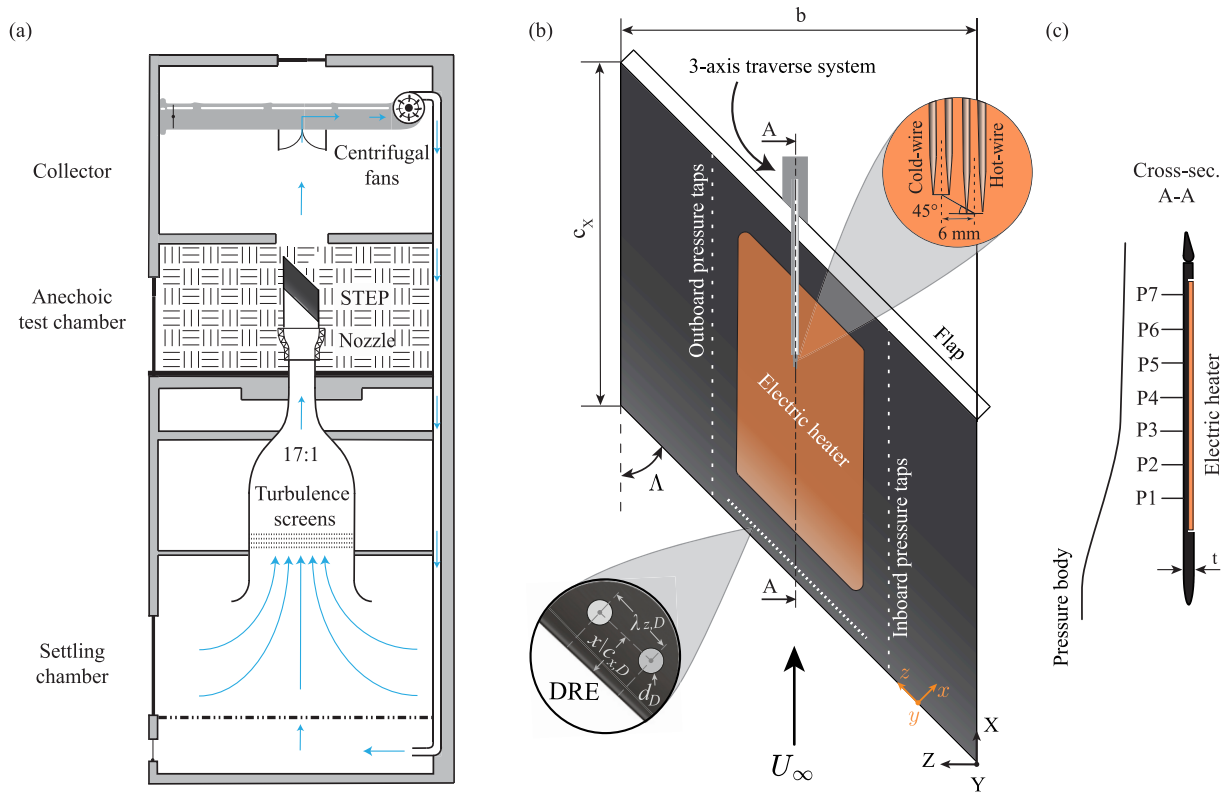

Fig. 1. (a) Cross-sectional schematic of the A-tunnel. Front (b) and side (c) view of the STEP model in real-world orientation (flow coming from bottom), showing its geometry and main components (cold- and hot-wire anemometry, DREs, pressure taps, and heating elements). Note that the dimensions in the sketch are not to scale.

tance Temperature Detector (RTD-Pt100)[3] and a digital barometer,[4] respectively.

The turbulence intensity (T_u) is measured using a single-wire probe aligned with the Z-axis and is defined as

$$T_u = \frac{1}{U_\infty}\sqrt{(1/2)(\overline{u'^2} + \overline{v'^2})}. \quad (1)$$

With the STEP model installed above the test section (Fig. 1a), and bandpass filtering the signal between 2 Hz $\leq f_{BP} \leq 2\times10^4$ Hz [18], the measured turbulence intensity is $T_u \approx 0.05\%$. Downs [21] recommended quantifying perturbations in streamwise vorticity to characterize the receptivity to T-CFI in different wind tunnel facilities. However, due to the lack of two-component HWA measurements, separate spectral distributions or T_u values for all three velocity components (u', v', and w') are not available. Nevertheless, the HWA spectral results presented in this work (e.g., Fig. 8a–c) clearly indicate that T-CFI are excited under the current freestream turbulence conditions. In particular, significant attenuation of the S-CFI saturation amplitude is observed, which motivated the inclusion of T-CFI in the CNPSE simulations. This observation is consistent with the experiments of Downs and White [18], where it was shown that even a modest increase in freestream turbulence from $T_u = 0.02\%$ to $T_u = 0.05\%$ resulted in a measurable attenuation of S-CFI and a significant amplification of T-CFI.

The experiments are performed with a new (in-house designed) Swept Transitional Experimental Platform (STEP), featuring a 45° swept flat plate with main geometrical parameters given in Table 1. A schematic of the STEP model and its main components is shown in Fig. 1(b–c). Further details can be found in [22]. The model features

Table 1
Geometric parameters of the swept flat-plate (STEP) model illustrated in Fig. 1(b–c).

Parameter	c_X	b	t	Λ
Value	848 mm	884 mm	20 mm	45°

two separate segments: $0 \leq X/c_X \leq 0.397$ (upstream plate) and $0.397 \leq X/c_X \leq 1$ (downstream plate). Care was taken to ensure that no gap formed between the two elements. Even so, to characterize any potential surface discontinuities at the plates' intersection ($X/c_X = 0.397$), surface profile measurements were taken using a Micro-Epsilon 3010-25BL laser scanner (resolution of 1.5 μm). No gap was detected during the experiments, and the maximum (forward-facing) step height measured was $h = 50$ μm, corresponding to $h/\delta^* = 0.075$, where δ^* is retrieved from the solution of the Compressible Boundary-Layer (CBL) equations at $X/c_X = 0.397$ in adiabatic conditions. Based on previous research (e.g., [23,24]), the effect of the present step height on S-CFI is deemed negligible.

The pressure distribution along the LE and the attachment line are modified using a trailing-edge (TE) flap, deflected approximately 18.16° upwards (towards the measurement side) during the experiments. The flow on the back of the flat plate is tripped by means of zig-zag tape to avoid undesired shedding at the TE.

A flexible top wall (pressure body in Fig. 1c) modifies the pressure distribution over the measurement side. The pressure outboard and inboard of the model is measured at two rows of 63 static pressure taps (126 in total) located at $z/b = 0.27$ from the midspan and connected to a set of differential pressure transducers.[5] The measured pressure

[3] Platinum resistance temperature detector (Pt100), 1/3 DIN (±0.1 degC at 20 degC).

[4] Barometer by Amphenol (amphenol-sensors.com), model: NPA-201, accuracy 0.01% of reading.

[5] Custom-made pressure scanner (NUB-System) equipped with Honeywell HSC series differential pressure transducers featuring ranges ±160, ±600 and ±2488 Pa with accuracy ±6, ±9 and ±25 Pa.

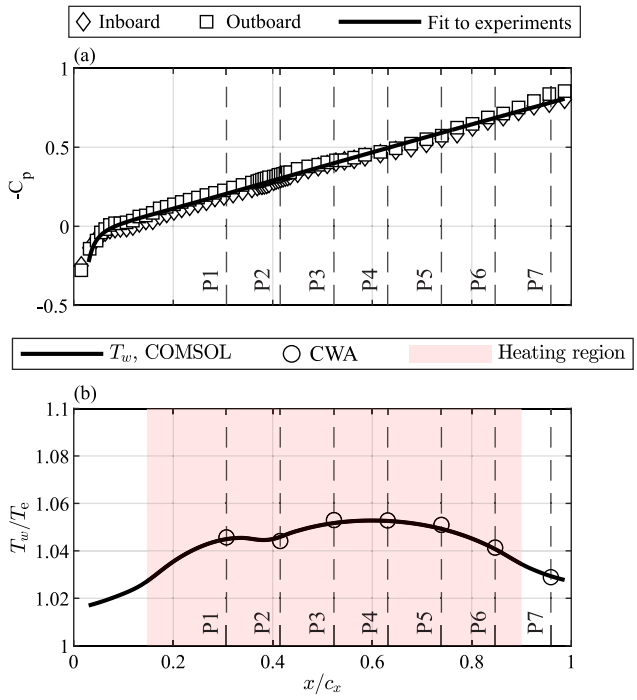

Fig. 2. (a) Pressure coefficient (C_p) obtained from outboard and inboard pressure tap measurements, along with a curve fit to the experimental data, which is used as the top boundary condition in the CBL equations. (b) Wall temperature distribution ($T_w(x)$) from CWA measurements and COMSOL simulations, with the latter used as wall boundary condition in the CBL simulations.

coefficient outboard and inboard is shown in Fig. 2(a), with C_p defined as

$$C_p = \left(p_{s,\text{tap}} - p_{s,\text{Pitot}}\right)/q_\infty \quad \text{with} \quad q_\infty = p_{t,\text{Pitot}} - p_{s,\text{Pitot}}, \tag{2}$$

where the subscript s and t denote static and total pressure, respectively. The measured pressure distribution, shown in Fig. 2(a), consists of a monotonically decreasing pressure (i.e., favorable pressure gradient) in the streamwise direction, which enhances the growth of CFI over TS waves. The overlap between outboard and inboard pressure measurements shown in Fig. 2(a) confirms the spanwise invariance condition and the validity of the 2.5D baseflow assumption in the region between the pressure taps.

Following the methodology described in previous experimental works on S-CFI-dominated transition (e.g., [25–27]), the amplitude and spanwise wavelength of the primary mode is conditioned using cylindrical Discrete Roughness Elements (DREs). The DREs are made out of an adhesive vinyl foil that determines the final DRE thickness (k_D). A CNC cutter is employed to manufacture the DREs using a digital template with the specific diameter (d_D) and spanwise element spacing (λ_z). The spanwise spacing (λ_z) and location (x_D) of the DREs are selected to match the wavelength and neutral point of the most amplified (primary) S-CFI mode, respectively. These parameters are obtained by solving the CLPSE for S-CFI on a baseflow extracted from the solution of the CBL equations under adiabatic conditions. The details of the numerical framework used to solve CBL and CLPSE are given in Section 2.2. The remaining DRE parameters (thickness and diameter) are carefully chosen in accordance to previous studies (i.e., [27]) to ensure linear receptivity. Table 2 presents the location and geometrical parameters of the DREs used in the experiments.

At the neutral point location ($x/c_x = 0.1$), where the DRE forcing is applied, the wall-temperature ratio is estimated to be $T_w/T_e \approx 1.022$ (Fig. 2b). Since the DRE configuration is unchanged between adiabatic and wall-heating conditions, S-CFI receptivity might be affected by

Table 2
DREs geometrical parameters. Here $c_x = c_X \cos\Lambda = 0.6$ m.

Parameter	λ_D	d_D	k_D	x_D/c_x
Value	10 mm	2 mm	125 μm	0.1

modifications of the BL with wall-heating. Purely based on predictions of stability theory, the neutral point is found to shift slightly upstream ($\Delta x/c_x \approx 0.0023$) under wall-heating. Thus, under wall-heating, the DREs are effectively placed downstream of the neutral point, where receptivity is known to be most effective [28,29]. Furthermore, wall heating increases the local displacement and momentum thickness (Fig. 3a), leading to a slight reduction of the roughness Reynolds number ($\text{Re}_k = |\boldsymbol{u}(k)|k/\nu(k)$) from $\text{Re}_k \approx 24$ (adiabatic) to $\text{Re}_k \approx 23$. Based on the trends reported by Zoppini et al. [27], this effect is also expected to reduce the initial S-CFI amplitude, rendering the present DRE configuration suboptimal under wall-heating conditions. Nevertheless, as will be shown later in this work, the direct effect of wall heating on the stability of S-CFI is significantly larger than the effect on receptivity factors near the LE. As such, the present experiments show consistently higher S-CFI amplitudes downstream of $x/c_x = 0.1$, indicating that the destabilizing influence of wall heating on S-CFI growth dominates over any disparity between adiabatic and wall-heating initial S-CFI amplitudes at receptivity.

The backside of the STEP model features two inserts (on the upstream and downstream plate) where two temperature-controlled silicon heaters[6] with electrical powers of 200 W and 400 W are placed to heat the upstream and downstream plates, respectively.

A key parameter for reproducing the current experiments using numerical tools is the wall temperature. The surface temperature is obtained at discrete streamwise points by extrapolating CWA temperature measurements towards the wall (refer to Section 2.1.1). To determine the temperature distribution along the entire centerline, a heat transfer simulation is performed in COMSOL Multiphysics based on the experimental conditions. In the simulations, the backside of the model is exposed to forced convection by turbulent flow at U_∞, except for the backside of the electric heater, which is insulated (zero heat flux). The front (measurement) side of the model is exposed to forced convection by laminar flow, modeled by imposing the heat transfer coefficient ($h(x)$) in COMSOL to match that obtained from the CBL solution. Finally, the heat flux delivered by the heaters is set to $Q_{w,\text{upstream}} = 1.6\ \text{kW m}^{-2}$ and $Q_{w,\text{downstream}} = 1.06\ \text{kW m}^{-2}$ to match the temperature values retrieved from CWA measurements. The wall temperature distribution obtained from COMSOL simulations and the CWA wall-temperature measurements are shown in Fig. 2(b). The wall temperature distribution obtained from COMSOL simulations is used throughout this work as the wall boundary condition for the CBL solver.

2.1.1. Hot-wire anemometry and cold-wire anemometry

The spatial and temporal evolution of the velocity within the boundary layer is retrieved using HWA. Notably, due to the imposed temperature gradient under non-adiabatic wall conditions, the HWA calibration and measurement procedure needs to be corrected based on the flow temperature at every sampling point. To do so, an additional wire probe operated in Constant Current Anemometry (CCA) mode at very low overheat ratios ($I = 0.5$ mA) is used as a cold-wire, denoted as CWA in what follows.

During the experiments, two Dantec Dynamics 55P15 boundary-layer probes are placed at 6 mm distance and forming a 45° angle (see Fig. 1b) to enable quasi-simultaneous velocity and temperature readings. During the post-processing, their relative distance is accounted

[6] Custom-made silicon heaters manufactured by the company Kracht (kracht.nl).

for to correct the HWA calibration with the CWA temperature at the corresponding location. The HWA probe is connected to a TSI IFA-300 constant temperature bridge, while the cold-wire probe is connected to a DISA 55M01 main unit equipped with a 55M20 constant current bridge module. The probes are translated in X, Y and Z directions using an automated traversing system[7] placed downstream of the STEP model (see inset in Fig. 1b), with a step resolution of 2.5 μm and a positional accuracy of 10 μm in all directions. Additionally, the sting supporting the dual-probe features an embedded accelerometer[8] to register any mechanical vibrations. This is key to separate the natural mechanical resonance frequencies of the supporting structure from any flow-related spectral content recorded by the HWA, as will be discussed later in Section 5.1.

The output voltage of the CWA scales linearly with temperature, significantly simplifying the calibration procedure [30]:

$$E = A_c + B_c T_a. \tag{3}$$

Both CWA and HWA probes are calibrated *in-situ*. The CWA calibration setup consists of a ceramic heating element with a positive temperature coefficient and a fan placed at the inlet of an insulated duct. The CWA probe is placed at the outlet of the pipe, in close proximity to an RTD-Pt100 sensor which records the temperature. The HWA probe is calibrated in the freestream by placing a Pitot-static tube in its proximity. The voltage signal obtained from the bridge is converted into a velocity signal using the calibration procedure described in [31], corrected with the mean temperature retrieved from CWA measurements.

Both HWA and CWA measurements are digitized at a sampling rate of $f_s = 51.2$ kHz for a total time of 2 s per measurement point. The cut-off frequency of the HWA bridge is determined by means of a square-signal test which yields a cut-off frequency of 17 kHz. Conversely, due to the low overheat ratio of the CWA, its frequency response is dependent on the thermal inertia of the wire, which for a wire with $d_w = 5$ μm and $l_w = 1.25$ mm is lower than 100 Hz [30]. For frequencies above 100 Hz, temperature fluctuations are strongly attenuated by the limited bandwidth of the CW sensor, although weak spectral signatures remain detectable. For example, during the late stages of transition, footprints of type-I secondary instabilities can still be identified in the temperature spectra. These observations suggest that, similar to the mean temperature field (see Fig. 3i–l), the unsteady temperature field behaves as a passive scalar, transported by the velocity fluctuations. In view of this passive behavior and the effective low-pass filtering of the sensor at frequencies above 100 Hz, in what follows, only time-averaged temperature measurements are presented.

Seven yz planes (i.e., parallel to the LE and normal to the surface) are scanned with HWA and CWA at different x stations to capture the spanwise organization and streamwise evolution of the CF vortices. Furthermore, measurements along an xz plane, within the range of $0.84 \leq x/c_X \leq 0.95$, are conducted at a fixed wall-normal location, $y/\delta_0^* = 3.70$, with $\delta_0^* = 0.6$ mm (obtained as defined in Section 2.3). These measurements are intended to provide insights into the final stages of the laminar-to-turbulent transition. The selection of the wall-normal location (y/δ_0^*) for the xz plane is chosen to approximately match the maxima of the type-I secondary instability [32].

The streamwise locations of CWA and HWA yz planes (P1 to P7) are illustrated in Fig. 1(c) and shown in Fig. 2. The measurement planes capture three spanwise wavelengths of the dominant primary S-CFI mode ($\lambda_z = 10$ mm). The yz planes are discretized into 54 uniformly distributed points in z direction (resolution of $\Delta z = 555$ μm along z), and 41 non-uniformly spaced points along the y direction, with higher grid resolution near the S-CFI maxima.

[7] Zaber X-LRQ-DE high-precision linear stages.

[8] Analogue Devices ADXL335.

The distance from the last HWA point to the wall is determined using a Taylor-Hobson microalignment telescope, featuring a resolution of 20 μm. During the post-processing, the wall distance measurement is refined using the strategy outlined in [33]. In this approach, a linear fit is applied to the near-wall boundary-layer measurements satisfying $U/U_e \leq 0.35$ to find the wall distance (i.e., $Q = 0$). However, in the two most downstream HWA planes ($0.85 \leq x/c_x \leq 0.95$) the meanflow is significantly modulated by the highly amplified S-CFI and the onset of laminar breakdown. In those cases, assuming a linear behavior towards the wall can yield higher uncertainty in the wall distance than the telescope resolution (i.e., $|\varepsilon| \leq 20$ μm). Therefore, for the last two HWA planes, only the optical wall measurement approach is used to establish the distance of the probe from the wall.

2.2. Numerical framework

In the present work, numerical solutions of baseflow and stability are presented alongside experimental results to further support the experimental findings and investigate the linear and nonlinear evolution of S-CFI under non-adiabatic wall conditions. The numerical methodology is divided in two parts. First, the CBL equations are solved to obtain the time-invariant and spanwise-invariant baseflow under a particular wall temperature distribution and freestream conditions. Secondly, the resulting perturbation solution from this baseflow is obtained using both CLPSE and CNPSE.

2.2.1. Compressible boundary-layer solver

The CBL equations for steady ($\partial/\partial t = 0$), flat-plate boundary-layer flows are solved. The boundary layer is assumed three-dimensional but spanwise invariant ($\partial/\partial z = 0$ with $w_\infty = w_e = cst.$). This simplified formulation is commonly referred to as infinite swept wing or 2.5D assumption. The final set of equations can be written as follows [34]:

$$\frac{\partial \rho u}{\partial x} + \frac{\partial \rho v}{\partial y} = 0, \tag{4}$$

$$\rho\left(u\frac{\partial u}{\partial x} + v\frac{\partial u}{\partial y}\right) = \rho_e u_e \frac{\partial u_e}{\partial x} + \frac{\partial}{\partial y}\left(\mu\frac{\partial u}{\partial y}\right), \tag{5}$$

$$\rho\left(u\frac{\partial w}{\partial x} + v\frac{\partial w}{\partial y}\right) = \frac{\partial}{\partial y}\left(\mu\frac{\partial w}{\partial y}\right), \tag{6}$$

$$\begin{aligned}\rho c_p\left(u\frac{\partial T}{\partial x} + v\frac{\partial T}{\partial y}\right) = &-u\rho_e u_e \frac{\partial u_e}{\partial x} + \frac{\partial}{\partial y}\left(k\frac{\partial T}{\partial y}\right) \\ &+\mu\left(\frac{\partial u}{\partial y}\right)^2 + \mu\left(\frac{\partial w}{\partial y}\right)^2,\end{aligned} \tag{7}$$

$$p = \rho R T, \tag{8}$$

where the subscript (e) denotes edge parameters (obtained at $y = \delta_{99}$), and R is the specific gas constant $R = 287\ \mathrm{J\,kg^{-1}\,K^{-1}}$. Note that there are effectively 5 unknowns (u, v, w, ρ, T) since the remaining parameters (μ and k) can be expressed as a function of temperature via Sutherland's law. At the wall, the no-slip ($u = 0$ and $w = 0$) and no-penetration ($v = 0$) conditions are specified together with isothermal ($T|_w = T_w$) or constant heat flux ($\partial T/\partial y|_w = 0$) conditions. In non-adiabatic conditions, the wall temperature distribution retrieved from the COMSOL simulation ($T_w(x)$, Fig. 2b) is used as isothermal wall condition.

The edge velocity distribution (u_e) is obtained from the experimental C_p (see Fig. 2a). To ensure smoothness in the numerical solution, the edge velocity distribution is expressed in terms of a polynomial fit of logarithmic basis, similar to Casacuberta et al. [35]:

$$\begin{aligned}\frac{u_e}{u_0}(x/c_x) = &\,0.0142\ln^3(x/c_x) + 0.1072\ln^2(x/c_x) \\ &+ 0.3161\ln(x/c_x) + 1.3566.\end{aligned} \tag{9}$$

where $u_0 = U_\infty \cos\Lambda = 11.12\ \mathrm{m\,s^{-1}}$ ($\Lambda = 45°$) and $c_x = 0.6$ m.

Additionally, the edge density (ρ_e) and temperature (T_e) are obtained from the edge velocity (u_e) using isentropic flow relations and assuming a specific heat ratio of $\gamma = 1.4$.

Following the formulation presented in [34], a Compressible Falkner-Skan Cooke (C-FSC) profile is set at the inflow ($x/c_x = 0.06$) given the local Hartree parameter ($\beta_H = 0.4$) and the wall temperature or the heat flux. Eqs. (4)–(8) are discretized using a second-order backward Euler (implicit) scheme in streamwise direction ($n_x = 1000$) and pseudo-spectral Chebyshev differentiation matrices in wall-normal direction with $n_y = 180$ Chebyshev polynomials. The collocation points in the y-direction are clustered near the wall to ensure that regions with strong shears are properly resolved.

2.2.2. Compressible linear and nonlinear parabolized stability equations

The compressible linear stability equations are obtained by distinguishing between a steady laminar solution (i.e., baseflow, $\boldsymbol{\Phi}$) and small perturbations on the velocity components, the density, and the temperature (i.e., disturbances, $\phi' = [u', v', w', \rho', T']$):

$$\phi = \boldsymbol{\Phi} + \phi'. \tag{10}$$

This decomposition is introduced into Eqs. (4)–(8); where the meanflow terms are subtracted; second-order streamwise derivatives are neglected; and invariant baseflow in z is assumed. In this work, quadratic disturbance terms (i.e., nonlinear terms) are retained to solve the evolution of finite-amplitude disturbances.

Analogous to Linear Stability Theory (LST), the total disturbance is assumed periodic in the temporal and spanwise directions. However, different to LST, the Parabolized Stability Equations (PSE) retain the streamwise dependency of the disturbances. In particular, it is assumed that the shape function changes slowly in x, while the phase can change rapidly in x [36]. In a nonlinear framework, the perturbation field is expressed as a sum of Fourier modes within the two invariant dimensions, namely time (t) and spanwise space (z), i.e.,:

$$\phi' = \sum_{m=-M}^{M} \sum_{n=-N}^{N} \hat{\phi}_{m,n}(\epsilon x, y) e^{i\left(\int_x \alpha_{m,n} \mathrm{d}x + \beta_n z - \omega_m t\right)}, \tag{11}$$

where $\epsilon = \mathrm{O}(\mathrm{Re}^{-1})$ [36]. Each (m, n) mode denotes one combination of temporal frequency and spanwise wavelength, M and N are the total number of truncated temporal and spatial Fourier modes, respectively. $\alpha_{m,n}$ represents the complex streamwise wavenumbers of a mode characterized by the angular frequency $\omega_m = m\omega_0$ and the spanwise wavenumber $\beta_n = n\beta_0$, where ω_0 and β_0 are the fundamental frequency and spanwise wavenumber, respectively. Finally, one crucial procedure is the so-called harmonic balancing, which aims to give a truncated system that describes the wave-triad interaction of harmonics [37,38].

Based on such a disturbance ansatz (Eq. (11)) and after performing harmonic balancing, the nonlinear system now reads:

$$\left\{ \boldsymbol{\mathcal{P}}\hat{\phi} + \boldsymbol{\mathcal{Q}}\frac{d\alpha}{dx}\hat{\phi} + \boldsymbol{\mathcal{L}}_x \frac{\partial \hat{\phi}}{\partial x} + \boldsymbol{\mathcal{L}}_y \frac{\partial \hat{\phi}}{\partial y} + \boldsymbol{\mathcal{L}}_{yy} \frac{\partial^2 \hat{\phi}}{\partial y^2} \right\}_{(m,n)} = \boldsymbol{\mathcal{N}}\boldsymbol{\mathcal{L}}_{(m,n)} \tag{12}$$

for each mode (m, n), where matrices $\boldsymbol{\mathcal{P}}$, $\boldsymbol{\mathcal{Q}}$, $\boldsymbol{\mathcal{L}}_x$, $\boldsymbol{\mathcal{L}}_y$, $\boldsymbol{\mathcal{L}}_{yy}$ are 5×5 linear operators which are the function of baseflow quantities $\bar{\boldsymbol{\Phi}}$, $\alpha_{m,n}$, ω_m, and β_n. The nonlinear forcing terms are denoted as $\boldsymbol{\mathcal{N}}\boldsymbol{\mathcal{L}}_{(m,n)}$.

The nonlinear system in Eq. (12) is discretized in a two-dimensional grid. The discretization used in wall-normal direction is analogous to the one employed in the CBL solver (refer to Section 2.2.1) containing 180 Chebyshev collocation points. In streamwise direction, a first order backward Euler (implicit) scheme with 600 equi-spaced grid points is used. The solutions of the compressible LST are used as the initial condition for the modes at the simulation inlet. Any new modes triggered by nonlinear forcing terms (i.e., right hand side of Eq. (12)) are introduced automatically by solving the local inhomogeneous equation once the forcing strength overtakes the threshold of $10^{-9}u_0$. For each mode (m, n), Eq. (12) is solved in a streamwise marching procedure and non-linear forcing terms are iteratively converged at each streamwise grid station. At the wall, a no-slip boundary condition is imposed for the disturbances as

$$\begin{aligned} y = 0, \quad & \hat{u} = \hat{v} = \hat{w} = \hat{T} = 0 \\ y \to \infty, \quad & \hat{u} = \hat{v} = \hat{w} = \hat{T} = \hat{\rho} = 0 \quad \text{for regular modes} \\ & \hat{u} = \partial\hat{v}/\partial y = \hat{w} = \hat{\rho} = \hat{T} = 0 \quad \text{for MFD} \end{aligned} \tag{13}$$

Mode (0,0) constitutes the meanflow distortion (MFD). This mode requires distinct boundary conditions for $\hat{v}$, facilitating an increase in boundary-layer thickness due to the sustained influence of MFD. Prior to initiating the $\alpha_{m,n}$-convergence process, an implicit nonlinear convergence loop is required to ensure the convergence of the nonlinear terms, analogous to the procedure described in [39].

Additionally, to ensure that the growth of the disturbance is uniquely captured in the phase term (i.e., $\int \mathrm{real}(\alpha_{m,n})\mathrm{d}x + \beta_n z - \omega_0 t$), a normalization condition is imposed on the shape function [36]:

$$\int \hat{\phi}^{\dagger} \frac{\partial \hat{\phi}}{\partial x} \partial y = 0. \tag{14}$$

where the superscript † symbolizes the complex conjugate. Therefore, in one marching step, $\alpha_{m,n}$ is iterated according to the normalization condition until the residual is lower than the threshold of $10^{-6}Re$.

In this study, simulations of nonlinear PSE on the conditions of the experiment are conducted for two distinct scenarios. First, only nonlinear interactions of S-CFI are considered; thus, the frequency ω_0 is fixed at zero in Eq. (11). A single spanwise fundamental mode (0,1), corresponding to a S-CFI with $\lambda_z = 10$ mm, is initialized at the inflow ($x/c_x = 0.06$). An iteration of the initial amplitude is performed until the maximum amplitude matches the value recorded in the experiment at the first measurement plane, P1 ($x/c_x = 0.3$, see Fig. 2). Here the fitted initial amplitude is denoted as A_{SCF}, defined later in Eq. (20). In total, 5 spanwise Fourier modes including MFD (0,0) are considered in all simulations. Tests with larger ensembles of modes have shown no significant difference.

Second, to assess how the presence and amplification of the T-CFI affect the saturation location and amplitude of the S-CFI, different amplitudes of the dominant T-CFI ($f = 130$ Hz) are introduced at the simulation inlet. Both the (0,1) and (1,1) modes are initialized simultaneously at the inflow. The amplitude of the S-CF mode (0,1) is fixed to the one found in the first case (i.e., without T-CFI), namely A_{SCF}. In contrast, the amplitude of the T-CF mode (1,1) is set to be a fraction of A_{SCF}, $A_{\mathrm{TCF}} = \kappa A_{\mathrm{SCF}}$ at plane P1 ($x/c_x = 0.3$). Previous studies (e.g., [40]) have demonstrated that the effect of T-CFI becomes evident when κ is larger than 3%. Therefore, an iteration of κ is carried out to find a good match of the saturation amplitude at $x/c_x \approx 0.85$ in the experiment. In these simulations, two frequency modes $M = 2$ and five spanwise modes $N = 5$ are selected. The optimal value found for κ is $\kappa_A = 13\%$ and $\kappa_H = 16\%$ for adiabatic and wall-heating cases, respectively.

Although small, these differences in κ can be expected to relate to modifications of T-CFI receptivity under wall-heating conditions, which are naturally present in the experiments but cannot be captured by CNPSE. To the best of the authors' knowledge, no systematic investigation of thermal effects on receptivity of T-CFI is available in past studies. Considering the limitations in the present measurements as well as the nature of the CNPSE approximation, it cannot be presently concluded whether the observed change in κ is caused by thermal modifications of receptivity to T-CFI upstream of $x/c_x = 0.06$. Nevertheless, to gauge the relative importance of such modification, additional CNPSE simulations were performed using the same initial T-CFI amplitude ($\kappa_H = \kappa_A = 13\%$). Results are not shown for conciseness. Under these conditions, the agreement between experiments and CNPSE leads to similar conclusions as those presented throughout this work with $\kappa_H = 16\%$. This indicates that, although receptivity modification effects may be present in the experiments, their influence on the observations derived from this study is expected to be limited.

In what follows, compressible linear solutions of PSE (CLPSE) are also presented and compared with compressible nonlinear PSE solutions (CNPSE) and experimental data. The CLPSE results are obtained from the CNPSE solver by omitting the nonlinear terms in Eq. (12).

2.3. Flow metrics and non-dimensional parameters

The experimental and numerical results presented herein have been normalized differently in x, y, and z directions. The streamwise coordinate (x) is non-dimensionalized based on the model chord orthogonal to the LE, i.e., $c_x = 0.6$ m. The wall-normal coordinate (y) is normalized by the displacement thickness under adiabatic conditions, $\delta_0^* = 0.6$ mm, obtained from CBL results at plane P1 ($x/c_x = 0.3$). The spanwise coordinate (z) is non-dimensionalized using the primary stationary CFI wavelength, $\lambda_z = 10$ mm. Velocity and temperature fields are normalized using the experimentally measured spanwise- and time-averaged external boundary-layer velocity ($\langle\overline{Q}_e\rangle_z$) and temperature ($\langle\overline{T}_e\rangle_z$).

In this work, numerical results are presented alongside HWA measurements. To guarantee a meaningful comparison between the two, numerical results will be expressed in terms of the resulting velocity component recorded by the hot-wire:

$$q = \sqrt{(u\cos\Lambda + w\sin\Lambda)^2 + v^2}, \tag{15}$$

where u and w correspond to the velocity components perpendicular and parallel to the LE, respectively. To ensure consistency between this definition and the experimental measurements, the traversing system is carefully aligned with the model's global coordinate system (X, Y, Z) during the experiments. This alignment ensures that the velocity components read by the hot-wire correspond to the projections of u and w onto the global X coordinate, and v onto the Y coordinate (see Fig. 1b).

The results obtained from the numerical solvers (e.g., baseflow, meanflow, and perturbation) must be transformed to the hot-wire aligned system (Eq. (15)) for effective comparison between experiments and stability solver results. In what follows, these are denoted as:

$$q = Q + q' \quad \text{and} \quad \bar{Q} = Q + q'_{(0,0)}, \tag{16}$$

where Q refers to the baseflow, q' to the perturbation, and $\bar{Q}$ to the meanflow in the hot-wire-aligned coordinates.

Similar to prior studies (e.g., [6,41,42]) the S-CFI amplitude, denoted as $\hat{q}_{\text{rms}}$, is herein defined as the root-mean-square (RMS) of the spanwise variations in the time-averaged flow field (or meanflow, $\overline{Q}$). Mathematically, this is expressed as:

$$\hat{q}_{\text{rms}}(y) = \sqrt{\langle\hat{q}^2\rangle_z}, \quad \text{with} \tag{17}$$

$$\langle\hat{q}^2\rangle_z = \frac{1}{N_z}\sum_{j=1}^{N_z}\left(\overline{Q}(y,z_j) - \langle\overline{Q}\rangle_z\right)^2, \tag{18}$$

where N_z denotes the number of discrete spanwise positions z_j, and $\langle\overline{Q}\rangle_z$ is the spanwise-averaged meanflow, defined as:

$$\langle\overline{Q}\rangle_z = \frac{1}{N_z}\sum_{j=1}^{N_z}\overline{Q}(y,z_j). \tag{19}$$

In the above definitions, $\hat{q}_{\text{rms}}$ contains information from all the spanwise disturbance modes (i.e., primary S-CFI and higher harmonics) but not from the MFD term ($q'_{(0,0)}$). The latter is instead contained in $\langle\overline{Q}\rangle_z$ added to the baseflow [43].

In this work, the amplitude (A) of the S-CFI is defined as the maximum value of $\hat{q}_{\text{rms}}(y)$ across the wall-normal direction, i.e.,

$$A = \max_y(\hat{q}_{\text{rms}}(y)), \tag{20}$$

For the analysis of the unsteady perturbation field, the power spectral density (PSD) of the HWA velocity fluctuations is computed and normalized following [25]:

$$P^* = \sqrt{\frac{\Delta f\ \text{PSD}(q')}{U_\infty^2}}, \tag{21}$$

where Δf denotes the frequency resolution. PSD(q') corresponds to the power spectral density of q', computed using Welch's Modified Periodogram method [44] using a Hann window. The signal is subdivided in 10 segments of 10 240 samples length overlapped by 50%, resulting into $\Delta f = 5$ Hz.

From the PSD data, the different frequency bands associated with relevant unsteady phenomena can be identified. To effectively isolate the velocity fluctuations associated with specific frequency ranges, the fluctuation signal ($q' = q - \overline{Q}$) is bandpassed at the identified frequency bands (BP) using an 8th order Butterworth filter. The standard deviation of the bandpassed signal ($\sigma_{q',\text{BP}}$) indicates the intensity of the velocity fluctuations at those frequencies. Mathematically, $\sigma_{q',\text{BP}}$ is defined as:

$$\sigma_{q',\text{BP}}(y,z) = \sqrt{\frac{1}{N_t}\sum_{i=1}^{N_t}\left[q'_{\text{BP}}(y,z,t_i)\right]^2}, \tag{22}$$

where N_t is the number of time samples, and q'_{BP} denotes the bandpassed fluctuation signal. For brevity, $\sigma_{q',\text{BP}}$ is denoted as σ_{BP} in what follows.

To effectively analyze the amplitude and growth of the unsteady perturbations, σ_{BP} is integrated over the HWA yz planes, following the approach outlined by Downs and White [18] and White and Saric [41]:

$$a_{\text{BP}} = \frac{1}{\langle\overline{Q}_e\rangle_z}\frac{1}{y_m}\frac{1}{z_m}\int_0^{y_m}\int_0^{z_m}\sigma_{\text{BP}}\mathrm{d}z\mathrm{d}y, \tag{23}$$

where y_m and z_m represent the extents of the integration domain in the wall-normal and spanwise directions, respectively.

2.4. Spectral linear stochastic estimation

In this study, the velocity fluctuations obtained from HWA measurements are influenced by mechanical vibrations of the sting (i.e. probe holder arm). When the HWA probe measures in regions with strong velocity gradients, oscillations of the sting cause the HWA probe to move across regions with large velocity variations, generating a spurious velocity fluctuation at the same frequency of the mechanical vibrations. In some cases, mechanical vibration frequencies coincide with those of flow instabilities, making it particularly difficult to distinguish between *physical* and *sting-induced spurious* fluctuations in the velocity signal. In what follows, sting-induced spurious velocity fluctuations will be denoted simply as *spurious* velocity fluctuations and the ones related to the flow problem of interest as *physical* for conciseness.

In an attempt to isolate *spurious* (q'_{spur}) from *physical* velocity fluctuations, the former are estimated from the signal of the accelerometer installed on the sting (a'_{acc}) by modeling the system as a first-order linear input–output relationship. This is achieved using Linear Stochastic Estimation (LSE), a technique widely employed in turbulence research to extract coherent structures in broadband flows (e.g., [45,46]). This approach assumes that spurious velocity fluctuations depend linearly on the accelerometer signal, which records the mechanical oscillations of the sting. This assumption implies negligible two-way coupling: structural vibrations do not significantly alter the flow, nor does the flow excite structural vibrations, e.g., vortex shedding around the HWA sting inducing structural vibrations. In this work, the strong coherence between accelerometer and HWA signals within specific frequency bands (see coherence, γ^2, peaks in Fig. 6d,e) supports this assumption.

Mathematically, the LSE can be expressed as

$$\hat{q}'_{\text{spur}}(t) = \int h(\tau)a'_{\text{acc}}(t-\tau)dt, \tag{24}$$

where $h(\tau)$ denotes a first-order transfer kernel, chosen to minimize the mean squared error between the true spurious velocity fluctuations (q'_{spur}) and the estimated one ($\hat{q}'_{\text{spur}}$) [47].

In this work, a spectral variant of LSE is used, namely Spectral Linear Stochastic Estimation (SLSE). This approach reduces complexity, as the convolution integral in Eq. (24) becomes a simple multiplication between the spectral input and the transfer function [47]. Fourier transforming Eq. (24) yields:

$$\hat{\mathcal{Q}}'_{\text{spur}}(f) = H_L(f)\mathcal{A}'_{\text{acc}}(f), \tag{25}$$

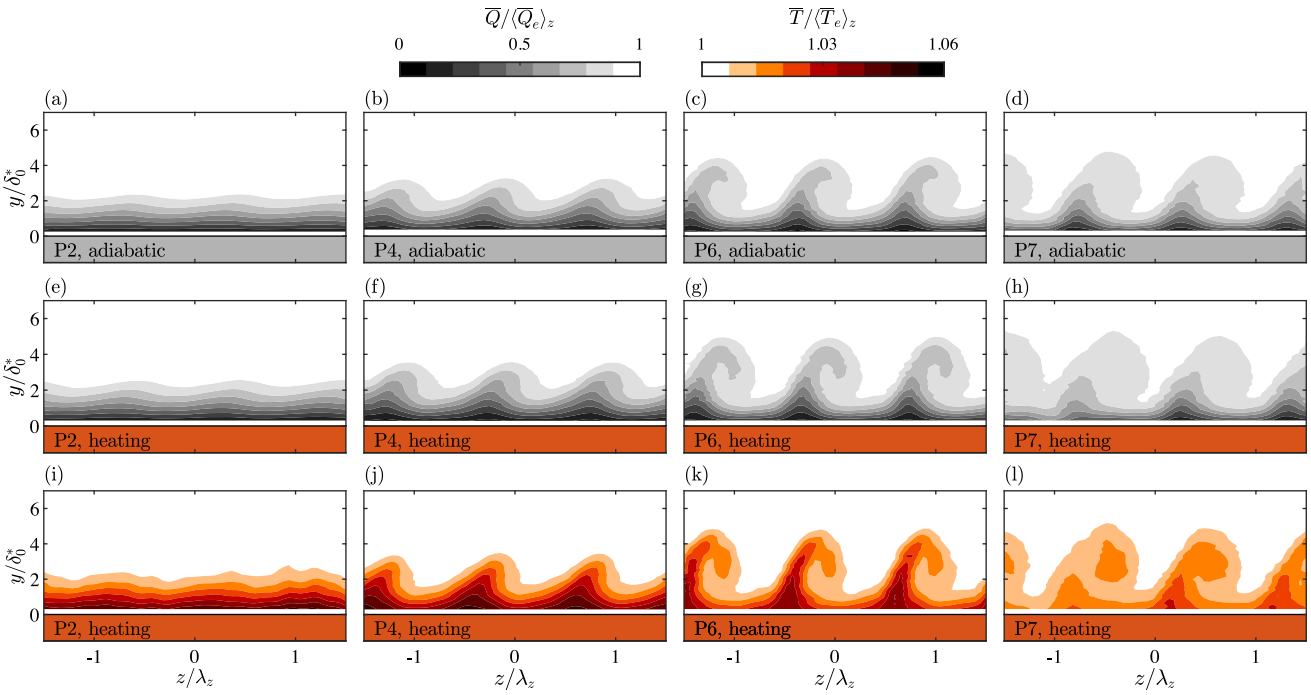

Fig. 3. Contours of the time-averaged velocity field retrieved from HWA at different yz planes in adiabatic (a–d) and wall-heating (e–h) conditions. (i–l) Contours of the time-averaged temperature field retrieved from CWA under wall-heating conditions. Positive z corresponds to the outboard side of the swept flat plate, with $z = 0$ indicating the model's midspan.

where $\hat{\mathcal{Q}}'_{\text{spur}}$ and $\mathcal{A}'_{\text{acc}}$ are the Fourier transforms of the estimated spurious velocity fluctuations ($\hat{q}'_{\text{spur}}$) and the accelerometer signal (a'_{acc}), respectively, and H_L is the complex-valued linear transfer kernel, defined as [46]:

$$H_L(f) = \frac{P_{\text{hwa,acc}}(f)}{P_{\text{acc}}(f)}, \tag{26}$$

where $P_{\text{hwa,acc}}$ denotes the cross-spectral density between HWA and accelerometer signal. Both cross- ($P_{\text{hwa,acc}}$) and power spectral densities (P_{hwa}) used to calculate H_L are computed using a standard segment-window-overlap-average procedure, using the same window and parameters defined in Section 2.3 when describing the Welch's periodogram method.

The time signal of the spurious velocity fluctuations ($\hat{q}'_{\text{spur}}$) is reconstructed performing an inverse Fourier transform of $\hat{\mathcal{Q}}'_{\text{spur}}$ using the overlap-add method [48]. Finally, the estimated physical vibrations ($\hat{q}'_{\text{corr}}$) can be obtained from the raw HWA signal (q'_{raw}) as:

$$\hat{q}'_{\text{corr}} = q'_{\text{raw}} - \hat{q}'_{\text{spur}}. \tag{27}$$

Results after applying this methodology to correct the velocity signal are presented at the end of Section 5.1.1.

3. Time-averaged flow field

The time-averaged HWA velocity fields at selected streamwise locations are presented in Fig. 3 under adiabatic (Fig. 3a–d) and wall-heating (Fig. 3e–h) conditions. The spanwise average of the velocity fields in Fig. 3(a–h) yields the velocity profiles shown in Fig. 4(c–f). Experimental results (symbols in Fig. 4) are compared with the baseflow solution from CBL (dashed lines in Fig. 4), together with the meanflow solution (solid lines in Fig. 4), computed by adding the meanflow deformation (MFD, $q'_{(0,0)}$) term from the CNPSE solution to the CBL baseflow solution. Additionally, the integral parameters obtained from the CBL baseflow solution (Q), and numerical and experimental meanflow ($\overline{Q}$) are presented in Fig. 4(a). Integral parameters are defined accounting for thermodynamic property variations across the boundary layer as:

$$\delta^* = \int_0^{\delta_{99}} \left(1 - \frac{\langle \overline{\rho}\,\overline{Q}\rangle_z}{\langle \overline{\rho}_e\,\overline{Q}_e\rangle_z}\right) \mathrm{d}y, \tag{28}$$

$$\theta = \int_0^{\delta_{99}} \frac{\langle \overline{\rho}\,\overline{Q}\rangle_z}{\langle \overline{\rho}_e\,\overline{Q}_e\rangle_z} \left(1 - \frac{\langle \overline{Q}\rangle_z}{\langle \overline{Q}_e\rangle_z}\right) \mathrm{d}y, \tag{29}$$

$$H_{12} = \frac{\delta^*}{\theta}, \tag{30}$$

At the most upstream streamwise stations (P1, P2, and P3), the velocity field presents minimal spanwise modulation (e.g., see P2 in Fig. 3a) due to the low amplitude of the S-CFI. At these planes, the time-averaged flow (or meanflow) closely resembles the baseflow, explaining the good agreement between CBL and experimental results both in terms of integral parameters (Fig. 4a for $x/c_x \leq 0.5$) and velocity profiles (Fig. 4c).

As the S-CFI propagates downstream and increases in amplitude, it induces a more pronounced spanwise modulation of the boundary-layer flow clearly reflected in the time-averaged velocity fields, as seen in Fig. 3 at planes P4, P6, and P7. The spanwise distortion of the boundary layer reflects the periodic organization and co-rotating motion of the S-CF vortices. This co-rotating motion creates two distinct regions in the CF vortex: the upwelling region (shoulder of the primary CF vortex), where low-momentum flow is displaced away from the wall, and the downwelling region, where high-momentum flow is moved towards the wall.

When the S-CFI reach significant amplitude, the vortices start to roll over their axis, forming a hook-like structure on the upper side of the vortex, particularly noticeable at plane P6 in Fig. 3(c,g). The modulation of the velocity field downstream of P6 is characteristic of S-CFI evolution at their later growth stages, just upstream of laminar breakdown, and has been previously documented in both experimental studies (e.g., [41,42]) and numerical simulations (e.g., [43,49]).

The substantial meanflow distortion caused by the amplified S-CFI leads to significant differences between experimental results and the

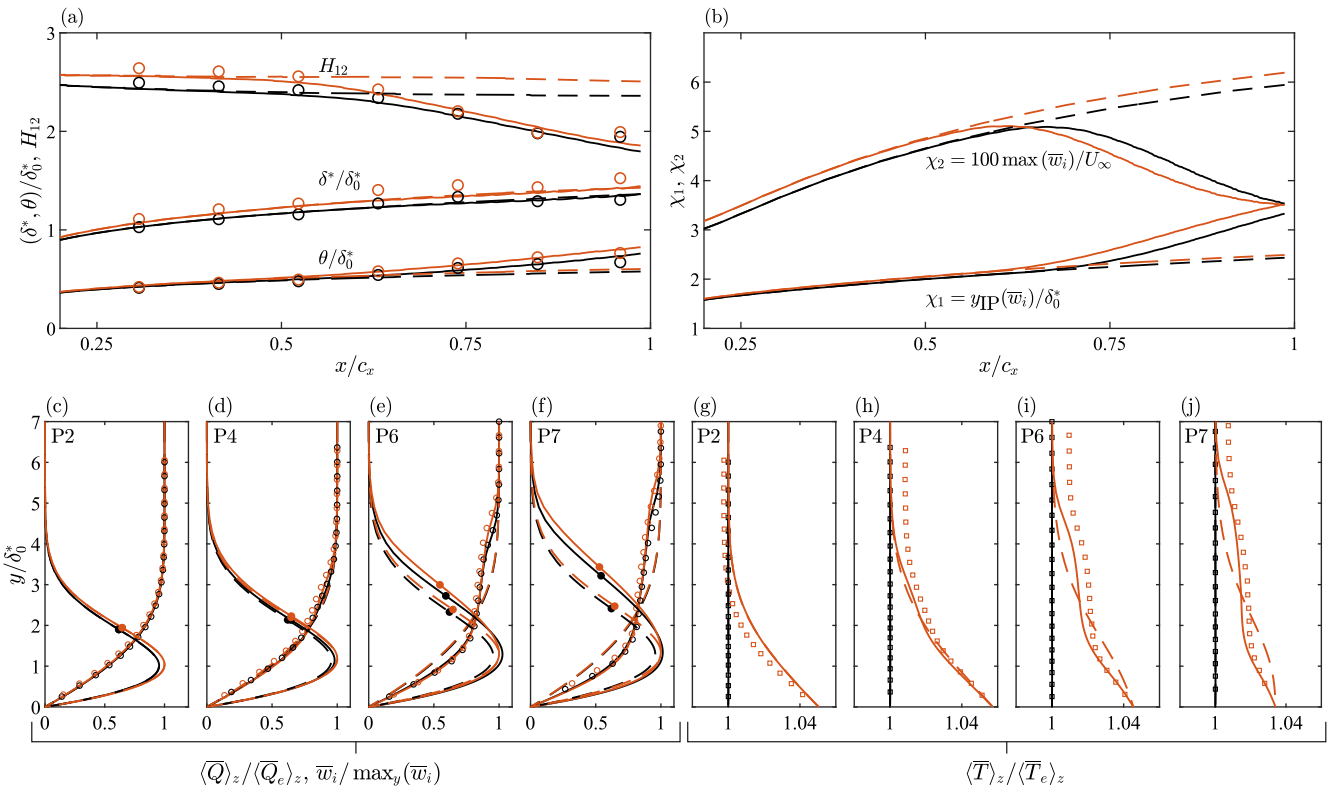

Fig. 4. (a) Boundary-layer integral parameters, i.e., displacement thickness (δ^*), momentum thickness (θ), and shape factor (H_{12}). (b) CF inflection point location ($y_{\mathrm{IP}}(\overline{w}_i)$) and CF maxima ($\max(\overline{w}_i)$). (c–f) meanflow and baseflow velocity profiles (Q and $\overline{Q}$, respectively) and CF profiles (w_i and $\overline{w}_i$, respectively). Filled symbols (• and •) in the CF profile indicate the location of the CF inflection point ($y_{\mathrm{IP}}(\overline{w}_i)$). (g–j) baseflow ($T$) and meanflow ($\overline{T}$) temperature profiles. All panels show time-averaged experimental data (open symbols, ∘), meanflow (solid lines, ——), and baseflow (dashed lines, - - -) numerical results. Wall-heating cases are shown in orange (e.g., ∘); adiabatic cases in black (e.g., ∘).

CBL baseflow solution, as seen in Fig. 4. These discrepancies become particularly evident from plane P4 onwards, as seen from integral parameters in Fig. 4(a) and velocity profiles in Fig. 4(e–f). In contrast, when non-linear interactions are accounted for by adding the MFD from CNPSE to the CBL baseflow profile, experimental and numerical results show excellent agreement (note agreement between solid lines, representing the meanflow numerical solution, and symbols, denoting experimental HWA data in Fig. 4c–j). Interestingly, the displacement thickness (δ^*) obtained from both baseflow and meanflow solutions exhibits similar values (Fig. 4a) in regions where the corresponding meanflow and baseflow velocity profiles present evident differences (e.g., Fig. 4e). This confirms that the changes observed in the velocity field result from a *redistribution* of fluid between high- and low-velocity regions, which effectively keeps the displacement thickness unchanged. This can also be visualized by the fact that the area enclosed by the difference between the baseflow and meanflow velocity profiles integrates to approximately zero (e.g., see Fig. 4e).

Fig. 3(i–l) show the time-averaged temperature fields retrieved from CWA measurements in wall-heating conditions. Comparison between the temperature fields in Fig. 3(i–l) and the corresponding velocity fields in Fig. 3(e–h) under wall-heating reveals a mirrored behavior between temperature and velocity. Regions where the S-CFI displaces high-momentum fluid from the freestream to low-momentum areas near the wall correspond to regions where low-temperature fluid is transported to high-temperature regions, and vice versa. Notably, the temperature field also exhibits the same hook-like shape associated with the roll-over motion of the CF vortices, as observed from plane P6 in Fig. 3(g,k).

The spanwise-average of the temperature fields presented in Fig. 3(i–l) yield the temperature profiles shown in Fig. 4(g–j). Notably, differences between experimental and numerical temperature profiles are largest at the freestream. This discrepancy arises from differences in the freestream temperature conditions between experimental and numerical results. During the long acquisition times required for measuring the high-resolution HWA planes, the ambient room temperature experienced fluctuations, resulting in freestream temperatures across all measurement planes that differed by up to ±1.5 degC. In contrast, the edge (freestream) temperature prescribed for the numerical simulations is set at a fixed value (i.e., T_0), defined as the average edge temperature obtained from CWA measurements across all measurement planes. As a result, discrepancies arise between the experimental and numerical results in the freestream region, as observed in Fig. 4(g–j).

Similar to the velocity field, in Fig. 4(i,j) it is observed that, at downstream streamwise stations, the baseflow solution alone (T) is insufficient to capture the experimental temperature profiles due to the distortion imparted by the strongly amplified S-CFI in these regions (see also T contours in Fig. 3k,l). In contrast, numerical mean temperature profiles ($\overline{T} = T + T'_{(0,0)}$) agree overall with experimental measurements. These observations highlight the need to account for the meanflow deformation also in the temperature field to accurately reproduce the experimental results.

Integral parameters in Fig. 4(a) demonstrate that the presence of a higher wall temperature renders significant modifications in the velocity field. These changes are particularly evident from results of the displacement thickness, which reveal a higher momentum deficit in the boundary layer with wall-heating. This can be explained by analyzing the boundary-layer equations at the wall [13]:

$$\left.\frac{\partial^2 u}{\partial y^2}\right|_{y=0} = \mathrm{Re}\,\frac{dp_e}{dx} - \frac{1}{\mu}\frac{\partial \mu}{\partial y}\left.\frac{\partial u}{\partial y}\right|_{y=0}, \tag{31a}$$

$$\left.\frac{\partial^2 w}{\partial y^2}\right|_{y=0} = -\frac{1}{\mu}\frac{\partial \mu}{\partial y}\left.\frac{\partial w}{\partial y}\right|_{y=0}. \tag{31b}$$

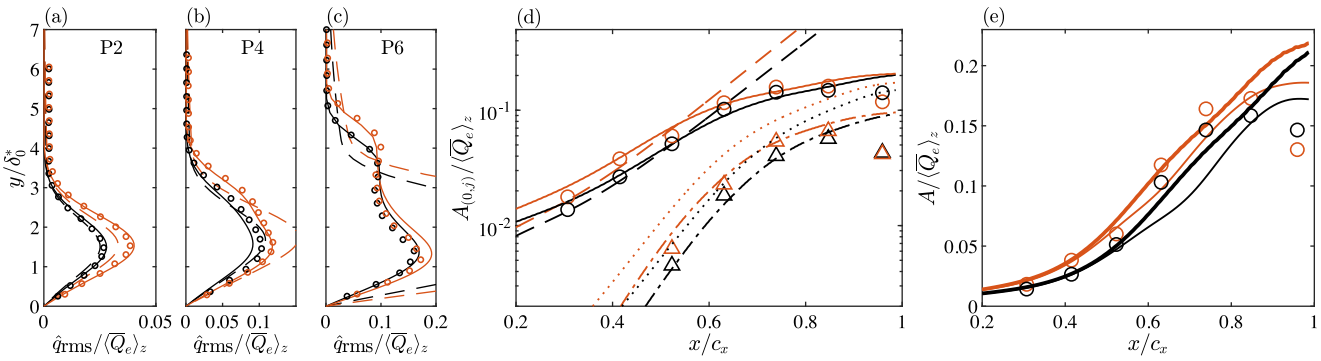

Fig. 5. (a–c) Total steady perturbation profile ($\hat{q}_{\rm rms}$) at different three HWA planes (P2, P4, and P6), obtained from experimental measurements (∘), CNPSE (——), and CLPSE (– – –). (d) Absolute perturbation amplitude (A, Eq. (20)) for different S-CFI modes. Fundamental S-CFI mode ($A_{(0,1)}$, $\lambda_z = 10$ mm): experiments (∘), CLPSE (– – –), and CNPSE (——). First S-CFI higher harmonic mode ($A_{(0,2)}$, $\lambda_z = 5$ mm): experiments (△) and CNPSE (–·–·–). MFD ($A_{(0,0)}$): CNPSE (·····). (e) Total steady perturbation amplitude (A, Eq. (20)) from experiments (∘), and CNPSE simulations with (thin solid line) and without (thick solid line) T-CFI interaction. In all panels: adiabatic in black and wall-heating in orange.

The flow case concerned herein is subject to a favorable pressure gradient, $dp_e/dx < 0$, which then yields an always negative $\partial^2 u/\partial y^2|_{y=0}$, i.e., no flow reversal is expected. Wall-heating results into a negative $\partial\mu/\partial y$ at the wall, rendering a less negative $\partial^2 u/\partial y^2|_{y=0}$ and a positive $\partial^2 w/\partial y^2|_{y=0}$ (Eq. (31)). In combination, these effects result into velocity profiles for both u and w which exhibit a higher momentum deficit, in agreement with experimental and numerical results shown in Fig. 4(a).

The net effect of increasing the momentum deficit within the boundary layer results in an increase of the CF component ($\max(\overline{w}_i)$) and an upward displacement of the CF inflection point ($y_{\rm IP}(\overline{w}_i)$), as shown in Fig. 4(b). In turn, this enhances the inviscid instability derived from this inflection point (i.e., the S-CFI), which can be expected to further destabilize the flow [13].

The above observations remain valid in the linear growth regime (i.e., upstream of plane P4), as evidenced by both baseflow (dashed lines in Fig. 4b) and meanflow (solid lines in Fig. 4b) results. However, as nonlinear effects become significant, the CF velocity component undergoes substantial modulation due to the influence of the high-amplitude S-CF vortex, analogous to the behavior observed for the streamwise velocity component. This modulation is characterized by a fuller CF velocity profile, with CF momentum being redistributed towards higher wall-normal locations (see Fig. 4e,f). As a result, the inflection point $y_{\rm IP}(\overline{w}_i)$ shifts further away from the wall compared to the baseflow solution. However, the increased wall-normal displacement of momentum results in a reduction of $\max(\overline{w}_i)$ relative to the baseflow solution. This behavior coincides with regions where the S-CFI amplitude starts to saturate.

Fig. 4(b) shows that, under wall-heating conditions, both $\max(\overline{w}i)$ and $y_{\rm IP}(\overline{w}_i)$ begin to deviate from the baseflow values at earlier streamwise locations compared to adiabatic results. This behavior suggests a more pronounced distortion of the meanflow under wall-heating, driven by the presence of higher-amplitude S-CFI. The following section will explore in detail the role of wall-heating in amplifying the S-CFI.

4. Steady perturbation content

Differences in S-CFI amplitude between adiabatic and wall-heating conditions become most evident when computing the S-CFI perturbation profile, introduced in Fig. 5(a–c). Results from CLPSE and CNPSE are presented together with experimental measurements for comparison.

Fig. 5(d) shows the amplitude in absolute terms, expressed as $A/\langle\overline{Q}_e\rangle_z$, for the MFD mode ($A_{(0,0)}$), the fundamental S-CFI mode ($A_{(0,1)}$), and the first harmonic ($A_{(0,2)}$) as obtained from experiments, CLPSE and CNPSE. For the experimental data, the decomposition of time-average flow field into the fundamental mode and harmonics is calculated by conducting a spatial FFT in z-direction at discrete y locations on a yz plane of the steady perturbation signal ($\hat{q}$), as outlined in similar works (e.g., [50]). The amplitude of each harmonic ($A_{(0,j)}$) is defined as the maximum value of the corresponding steady perturbation profile, as given by Eq. (20). The reason for defining the amplitude (A) as the maximum of the $\hat{q}_{\rm rms}$ profile instead of as the integral over y is two-fold: (1) it ensures consistent comparison between numerical and experimental results, the latter spanning a more limited y range which would otherwise require extrapolation to integrate the $\hat{q}_{\rm rms}$ profile along the numerical y grid; and (2) the definition aligns with previous experimental studies, where values for the saturation amplitude are typically reported as the maximum value of the S-CF vortex normalized by the external velocity, i.e. A/Q_e (e.g., [51]). Finally, note that experimental values for $A_{(0,2)}$ are not shown in Fig. 5(d) upstream of P3 because their amplitude values are comparable to the signal-to-noise ratio of the HWA measurements, making them indistinguishable from measurement noise.

Upstream of $x/c_x \approx 0.5$, the growth of the S-CFI remains linear. This is evidenced in Fig. 5 by the close agreement between CLPSE, CNPSE, and experimental results in terms of both the total steady perturbation profile ($\hat{q}_{\rm rms}$, Fig. 5a) and the fundamental mode's amplitude evolution ($A_{(0,1)}$, Fig. 5d) under both wall-heating and adiabatic conditions. Furthermore, CLPSE, CNPSE, and experimental results indicate that wall-heating promotes the destabilization of S-CFI within the linear regime.

Downstream of $x/c_x \approx 0.5$, deviations start to emerge between experimental and CLPSE results. Conversely, CNPSE results are able to capture the modifications observed in the experimental perturbation profile (see Fig. 5b) and the saturation of the fundamental S-CFI mode (see Fig. 5d). The divergence of CLPSE results from CNPSE and experimental data is attributed to the onset of nonlinear interactions, as evidenced by the amplification of the MFD and the second ($A_{0,2}$) S-CFI mode downstream of $x/c_x \approx 0.5$ (see Fig. 5d). Despite the growth of these harmonics, the amplitude of the fundamental S-CFI mode remains significantly larger than its harmonics. Specifically, the first harmonic mode amplitude never exceeds 35% of the fundamental mode amplitude (Fig. 5d). Additionally, no growth of subharmonic modes (i.e., longer wavelengths than λ_z) is detected in the experiments. These findings align with previous experimental studies conducted under similar DRE forcing conditions, where the DRE wavelength matches that of the primary S-CFI mode (e.g., [18,50]).

In agreement with previous experimental (e.g., [50,52]) and numerical studies (e.g., [32,43]), saturation of the S-CFI amplitude ($x/c_x >$

0.7 in Fig. 5d,e) is accompanied by the development of a secondary lobe in the steady disturbance profile (see $\hat{q}_{\mathrm{rms}}$ in Fig. 5c). This is a characteristic feature of S-CFI development under stages of strong non-linear interactions. This secondary lobe manifests as a consequence of the roll-over of the CF vortices, as also seen from velocity contours in Fig. 3(g) in these experiments, and coincides with amplitude growth saturation [53].

Comparison between adiabatic and wall-heating absolute amplitude values in Fig. 5(d) reveals a consistently higher amplitude of the fundamental S-CF mode and higher harmonics under wall-heating. Overall, the growth development under wall-heating obeys an analogous behavior as in adiabatic conditions: an initially linear regime, later non-linear interactions, amplitude saturation, and eventually, laminar breakdown (the latter evidenced by the drop in amplitude from $x/c_x \approx 0.85$ to $x/c_x \approx 0.96$, see Fig. 5d,e). However, all stages occur farther upstream under wall heating due to the enhanced amplitude levels. This is evidenced by the more pronounced development of the second lobe in $\hat{q}_{\mathrm{rms}}$ (Fig. 5c) and the earlier saturation of the S-CFI amplitude (Fig. 5e) in the wall-heated case. These findings are consistent with previous observations derived from the time-averaged flow fields, which show that wall heating increases displacement thickness and amplifies the CF component, yielding a more unstable baseflow solution for S-CFI [13].

Similar to Fig. 5(d), Fig. 5(e) shows the streamwise evolution of the total S-CFI perturbation amplitude obtained from both experiments and CNPSE. In this case, two different CNPSE solutions are compared: one that solves only for stationary CFI modes, and another that solves for both stationary and traveling CFI modes, following the methodology outlined in Section 2.2. Note that, different from Fig. 5(d), results are plotted on a linear instead of logarithmic scale to effectively visualize regions of high amplitude values, where the S-CFI reaches saturation.

Two important observations can be drawn from the results shown in Fig. 5(e). First, when CNPSE simulations account only for stationary CFI modes, they fail to reproduce the amplitude saturation observed experimentally between planes P5 and P6 (i.e. $0.74 \leq x/c_x \leq 0.85$, Fig. 5e). In contrast, when finite-amplitude traveling CF modes are introduced at the inflow, CNPSE can capture the onset of S-CFI saturation measured in the experiments near plane P6. Similar observations have been reported in the works of Malik et al. [53], Bippes [50], and Hein [54], investigating the interaction between stationary and traveling CFI modes employing NPSE. The authors report attenuation in the growth of S-CFI modes growth due to the interaction with moderate-amplitude T-CFI modes, e.g., see Fig. 1 in [54] and Fig. 18[9] in [53]. The inability of NPSE to capture the S-CFI saturation amplitude when only S-CFI modes are resolved suggests that moderate-amplitude T-CFI have a non-negligible contribution in the present experiments. These unsteady modes are likely excited by the low-frequency content of the freestream turbulence in the wind tunnel [50]. Further evidence supporting the existence of moderate-amplitude T-CFI will be presented in Section 5.2. Finally, it should be noted that downstream of $x/c_x \approx 0.85$, both CNPSE variants fail to reproduce the decay of the total perturbation amplitude A, due to the increasing influence of secondary instabilities and eventual loss of spanwise coherence in the flowfield due to laminar breakdown, which are not accounted for in the current NPSE framework.

The second observation that can be drawn from Fig. 5(e) concerns the higher S-CFI saturation amplitude observed under wall-heating compared to adiabatic conditions. Fig. 5(e) shows that, right before laminar breakdown (i.e., at plane P6), the S-CFI amplitude is lower under adiabatic conditions ($A/\langle\bar{Q}_e\rangle_z = 0.159$) than under wall-heating ($A/\langle\bar{Q}_e\rangle_z = 0.175$). These values are consistent with the saturation amplitudes reported by Downs and White [18] for a freestream turbulence intensity of approximately $T_u \approx 0.05\%$, close to the T_u present in these experiments.

According to previous studies (e.g., [18,50]), and as previously discussed, lower S-CFI saturation amplitudes are typically observed in facilities with higher levels of freestream turbulence. As explained by Bippes [50], higher T_u levels promote higher-amplitude T-CFI, leading to stronger interactions with stationary modes, which attenuate S-CFI and eventually reduce its saturation amplitudes. However, as previously discussed, the present results reveal the opposite trend: wall-heating substantially enhances T-CFI growth (as will be further proved by results of Section 5.2), yet the S-CFI saturation amplitude is higher under wall-heating than under adiabatic conditions. These observations indicate that the increased S-CFI saturation amplitude is a direct consequence of wall-heating. This further suggests that the effect of wall heating dominates over the attenuating effect of higher-amplitude T-CFI on saturation amplitude. This behavior is also captured by the CNPSE simulations (Fig. 5e), providing confidence in the experimental observations. A plausible explanation for this behavior is that wall-heating modifies the underlying flow (both mean flow and perturbations), leading to a different equilibrium state, as suggested by Koch et al. [55]. In particular, Koch et al. [55] demonstrate that variations in saturation amplitude can be traced to different equilibrium solutions, which depend on the characteristics of the basic flow. The results presented in this study demonstrate that wall heating visibly modifies the mean flow and perturbation field, giving rise to a different equilibrium solution. In the particular case of wall-heating, this new equilibrium solution can sustain higher perturbation energy than the adiabatic equilibrium solution, manifesting as a higher saturation amplitude in both experiments and CNPSE.

5. Unsteady perturbation content

In this section, the spectral content of the HWA signal is presented to identify the nature (whether physical or spurious) of the distinct velocity fluctuations recorded during the experiments. Next, after establishing the characteristic frequency ranges associated with T-CFI, type-III, and type-I modes, the influence of wall-heating on their respective growth and spatial development is examined. Finally, the impact of wall heating on the late stages of laminar-to-turbulent transition is investigated.

5.1. Spectral characterization

The strong distortion induced by the high-amplitude S-CF vortices on the boundary-layer flow creates persistent spanwise and wall-normal velocity gradients. In turn, these high velocity shears foster the formation of secondary CFI. Consequently, when aiming to identify secondary CFI, it is instructive to analyze the spatial development of spanwise and wall-normal shears (e.g., [32,56]). In this work, the latter are computed from the time-averaged HWA velocity fields ($\bar{Q}$) and expressed in non-dimensional form as:

$$G_y = \frac{\delta_0^*}{\bar{Q}_e}\frac{\partial \bar{Q}}{\partial y}, \text{ and} \tag{32}$$

$$G_z = \frac{\delta_0^*}{\bar{Q}_e}\frac{\partial \bar{Q}}{\partial z}. \tag{33}$$

In this section, the spectral content of the HWA signal in regions of strong velocity shears are inspected in order to:

1. Distinguish between physical and spurious (i.e., sting-induced) spectral signatures (refer to Section 2.4).
2. Identify the characteristic frequency band and spatial organization of pertinent secondary instability modes.

[9] Fig. 18 in [53] shows differences in growth rate from NPSE with and without accounting for S-CFI and T-CFI interactions. In particular, the difference between lines "2" and "4" represents how the growth rate is modified when T-CFI interactions are accounted for.

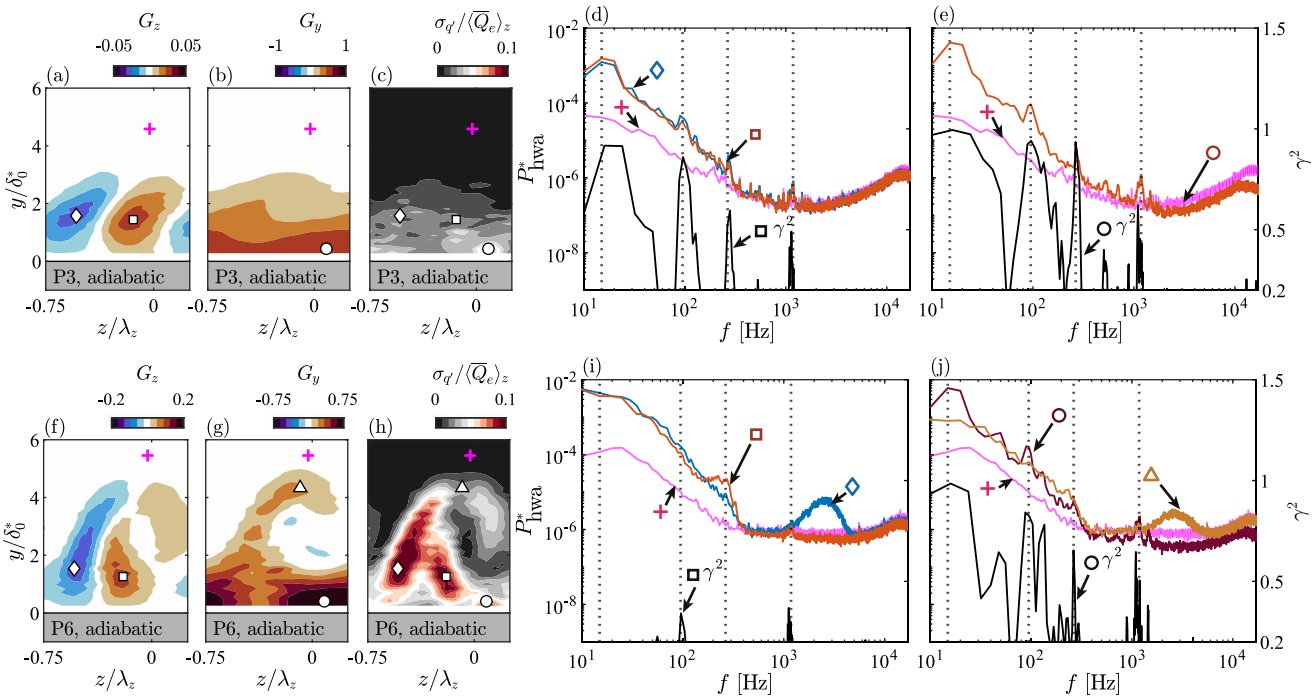

Fig. 6. (a–c, f–h) Contours of spanwise shear (G_z, a and f), wall-normal shear (G_y, b and g), and standard deviation of HWA velocity fluctuations ($\sigma_{q'}$, c and h) at planes P3 and P6 in adiabatic conditions. (d-e, i-j) Non-dimensional spectra of HWA velocity fluctuations (P^*_{hwa}) at positions of maximum (□) and minimum (⋄) spanwise shear (d and i) and maximum (△ and ○) wall-normal shear (e and j). Freestream PSD signal (+, magenta line) and coherence spectra (γ^2, black line). Symbols denote locations of PSD signal extraction, indicated in (a–c) and (f–h) contours.

5.1.1. *Spurious velocity fluctuations*

To distinguish between spurious and physical velocity fluctuations (defined in Section 2.4), it is instructive to analyze the coherence (γ^2) between the accelerometer and HWA signals. The accelerometer captures the mechanical vibrations of the HWA holder and supporting structure (i.e., sting), while the HWA signal encodes both physical and spurious (i.e., sting-induced) velocity fluctuations. High coherence in specific frequency bands suggests a consistent phase relation between the signals, indicating that the velocity fluctuations captured by the HWA are largely driven by the mechanical vibrational motion of the sting.

Fig. 6 presents the Power Spectral Density (PSD) of the HWA signal and the magnitude squared coherence (γ^2) between the HWA and accelerometer signals, calculated as [57]:

$$\gamma^2(f) = \frac{|P_{\mathrm{hwa,acc}}(f)|^2}{P_{\mathrm{hwa}}(f) \cdot P_{\mathrm{acc}}(f)}, \tag{34}$$

where $P_{\mathrm{hwa,acc}}$ is the cross power spectral density of the accelerometer and HWA signals, and P_{hwa} and P_{acc} are their respective power spectral densities, calculated using Welch's periodogram method. The signal preprocessing steps performed prior to applying Welch's periodogram method are detailed in Section 2.3. Note that in Fig. 6, P^*_{hwa} denotes the normalized PSD of the HWA signal, as defined in Eq. (21).

Fig. 6(d,e) show PSD and coherence (γ^2) results at $x/c_x \approx 0.52$ (plane P3), where the perturbation development remains largely linear (see Fig. 5d). At this location, the spectral content of the HWA signal (P^*_{hwa}) exhibits similar behavior across different regions of the velocity field. This becomes evident by comparing results for $P^*_{\mathrm{hwa}}(f)$ (Fig. 6d,e) at the three probe positions marked in Fig. 6(a–c). Accelerometer and HWA signals present high coherence (γ^2, see black curve in Fig. 6d,e) at several frequency bands, centered around $f = [15, 95, 265, 1180]$ Hz (see vertical dotted lines in Fig. 6d,e). These peaks are also present in the accelerometer spectra during forced vibration tests without flow (i.e., hammer tests, not shown here), confirming that they correspond to the natural resonance frequencies of the HWA sting. Consequently, velocity fluctuations measured at plane P3 are primarily caused by oscillations of the HWA sting along the y-axis, rather than to the onset of secondary instabilities.

In this work, Spectral Linear Stochastic Estimation (SLSE) is used in an attempt to remove spurious velocity fluctuations from the HWA signal, caused by sting-induced vibrations. Details on the methodology employed are outlined in Section 2.4.

Fig. 7(a–b) shows the PSD of the corrected (corr(P^*_{hwa}), thick line in Fig. 7) and raw HWA signal (P^*_{hwa}), extracted at a location of strong wall-normal shears, indicated by a circular marker in Fig. 7(c–f). Amplitude differences between corr(P^*_{hwa}) and P^*_{hwa} are larger across the frequency bands where maximum coherence (γ^2) was observed in Fig. 6(d,e). The latter is expected since, combining Eqs. (34), (26), (27), it can be demonstrated that the PSD of the corrected signal can be expressed as a scalar product of the coherence [46]:

$$\mathrm{corr}(P^*_{\mathrm{hwa}}) = (1 - \gamma^2) P^*_{\mathrm{hwa}}. \tag{35}$$

Fig. 7(c–f) present the bandpass-filtered RMS contours (σ_{BP}) of uncorrected (raw) and corrected HWA signals within the frequency range 80 Hz $\leq f \leq$ 140 Hz. This frequency range is of particular interest because it contains strong sting-induced vibrations (high levels of γ^2, Fig. 6d,e) and also constitutes a spectral band where CLPSE predicts strong amplification of T-CFI (see overlaid N-factor curves in Fig. 7a,b).

Fig. 7(c,e) show contours of the bandpass-filtered (80 Hz $\leq f \leq$ 140 Hz) velocity fluctuations before correction. RMS levels (σ_{BP}) become more prominent inside the boundary layer, where wall-normal velocity shears (contour lines in Fig. 7c,e) are stronger, and vanish in the freestream. These observations suggest that these fluctuations are related to sting-induced vibrations, as also identified in the work of Eppink and Wlezien [19].

Compared to uncorrected σ_{BP} contours (Fig. 7c,e), corrected contours (Fig. 7d,f) reveal a significantly different spatial distribution, with high-RMS regions now located farther away from the wall, on the inner side of the upwelling region. Additionally, the contours exhibit a spanwise modulation aligning with the primary S-CFI wavelength.

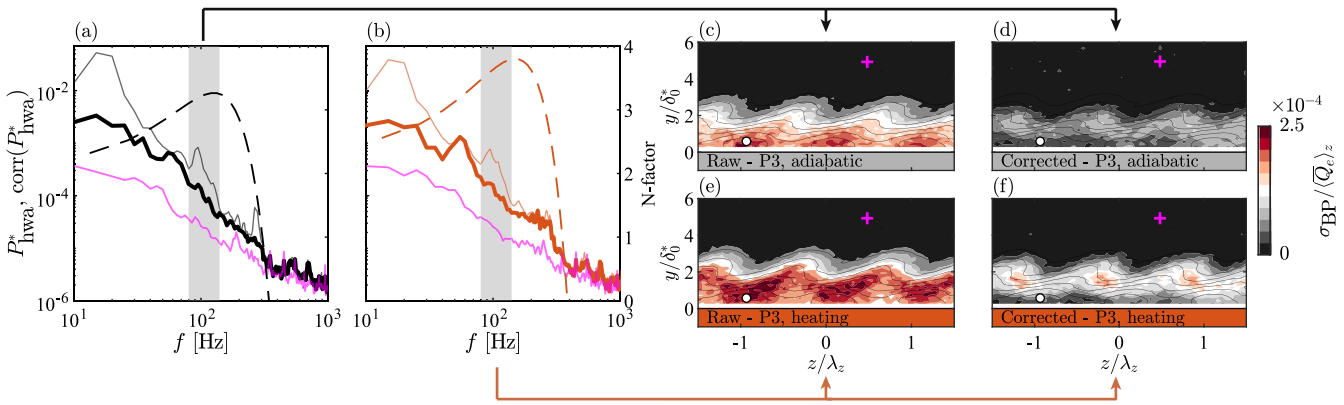

Fig. 7. (a–b) Non-dimensional PSD of raw (P^*_{hwa}, thin line) and corrected (corr(P^*_{hwa}), thick line) HWA signals, extracted at the location marked by ∘ in the contours. Freestream PSD signal (+, magenta line) and N-factor from CLPSE (– – –). The gray band indicates the spectral range $80 \leq f \leq 140$ Hz. (c–f) Contours of raw (c,e) and corrected (d,f) bandpass-filtered signals within $80\ \mathrm{Hz} \leq f \leq 140\ \mathrm{Hz}$. Black contour lines represent the wall-normal velocity shears (G_y). All panels show results at plane P3, with adiabatic results in black and wall-heating in orange.

This spatial distribution is characteristic of T-CFI at their early growth stages (e.g., [53]).

Notably, σ_{BP} levels from Fig. 7(d) and (f), related to T-CFI, reveal higher velocity fluctuations under wall-heating than in adiabatic conditions. The role of wall-heating in amplifying T-CFI will be further investigated later in Section 5.2.

Overall, the results in Fig. 7 underscore the importance of correcting the HWA signal to mitigate the influence of sting-induced vibrations, which can otherwise mask other instability mechanisms occurring within the same spectral band.

5.1.2. Physical velocity fluctuations

To identify the spectral characteristics and frequency band of secondary instabilities, the spectral content of the HWA signal is analyzed at a further downstream plane, P6, where secondary instability development becomes significant. Results for this plane are presented in Fig. 6(f–j).

Different from observations at plane P3, regions of strong spanwise shears (G_z, Fig. 6f) share an evident spatial correlation with regions of high velocity fluctuations ($\sigma_{q'}$, Fig. 6h). Similar observations are reported in previous works (e.g., [32,56]), where the presence of strong spanwise velocity shears is observed to foster the growth of secondary instabilities, manifested as regions of high $\sigma_{q'}$ in Fig. 6(h).

Fig. 6(i) shows the velocity spectra at both outer (see ⋄ symbol in Fig. 6f) and inner (see □ symbol in Fig. 6f) sides of the upwelling CF region. Note that, different from observations at plane P3, spectral peaks associated with sting-induced velocity fluctuations are masked under the considerably higher energy content of the physical velocity fluctuations (e.g., note the absence of P^*_{hwa} peaks at $f = 10$ Hz and $f = 95$ Hz from plane P6, in Fig. 6i, compared to plane P3, in Fig. 6d). This is also confirmed by the lower magnitude of γ^2 at these frequencies, e.g., at $f = 95$ Hz, $\gamma^2 = 0.96$ at plane P3, whereas it drops to $\gamma^2 = 0.34$ at plane P6.

The HWA spectral content at the outer side of the upwelling region (see blue curve in Fig. 6i) exhibits elevated energy within the high-frequency range, at $f = [1500, 4000]$ Hz. The frequency characteristics and spatial location of these velocity fluctuations are indicative of type-I secondary instabilities [41]. Bonfigli and Kloker [49] show that the high-frequency content associated with type-I secondary instabilities is attributed to the development of inviscid Kelvin–Helmholtz instabilities over the upwelling side of the CF vortex, as a result of the high spanwise shears. Conversely, the velocity spectra at the inner side of the upwelling region (see orange curve in Fig. 6i) shows higher energy content within the low-frequency regime, at $f = [150, 400]$ Hz. These fluctuations are characteristic of type-III secondary instability development, emerging from the interaction between stationary and traveling CFI [53].

In contrast to spanwise shears (G_z, Fig. 6f), topological similarities between regions of high wall-normal shear (G_y, Fig. 6g) and high $\sigma_{q'}$ regions from Fig. 6(h) are less evident. Two regions of high wall-normal shear are identified from Fig. 6(g). The first region appears near the wall (∘ symbol in Fig. 6g), driven by the high velocities associated with the down-welling motion of the CF vortex. HWA spectral results extracted at this point are shown in Fig. 6(j) (see results associated to ∘ symbol). The spectral content reveals significant similarities to PSD results observed at plane P3, i.e., P^*_{hwa} exhibits amplitude peaks at frequencies of strong coherence (i.e., high γ^2) between HWA and accelerometer signals. In line with the discussion presented in Section 5.1.1, these observations suggest that elevated $\sigma_{q'}$ values in this high G_y near-wall region potentially originate from vibrations of the HWA sting [19], and not from physical flow structures.

The second region of high wall-normal shear in Fig. 6(g) is situated at the crest of the upwelling CF region, close to where type-I secondary instabilities also develop (see △ symbol in Fig. 6g). In this region, previous experimental (e.g., [41]) and numerical (e.g., [49]) studies report the development of so-called type-II secondary instability (y-mode in [56]). However, Fig. 6(h) shows no clear signature of high $\sigma_{q'}$ values in this region. PSD results in this region (see results associated to △ symbol in Fig. 6j) reveal an increase in energy within the same frequency range previously ascribed to type-I modes (i.e., $f = [1500, 4000]$ Hz). Despite their spatial proximity, type-II secondary instabilities can be distinguished from type-I because they manifest at distinctly higher frequencies [41]. In the present experiments, type-II instabilities cannot be distinguished from the spectral signatures in Fig. 6(j). The absence of type-II secondary instabilities has also been reported in previous experimental investigations by White et al. [17], as well as DNS computations by Wassermann and Kloker [32]. Furthermore, Bonfigli and Kloker [49] have reported discrepancies in the amplitude predicted by Secondary Linear Stability Theory (SLST) for type-II modes compared to the one obtained from DNS and experimental results. White and Saric [41] and Malik et al. [56] attribute the absence of type-II instabilities to differences in the receptivity process across different experiments or DNS studies. Namely, the lower energy content of freestream turbulence at high frequencies (a characteristic feature of the current wind tunnel facility) would tend to favor the receptivity and amplification of type-III and type-I instabilities in comparison to type-II instabilities [41]. This could explain the absence of type-II instabilities in the present experiments.

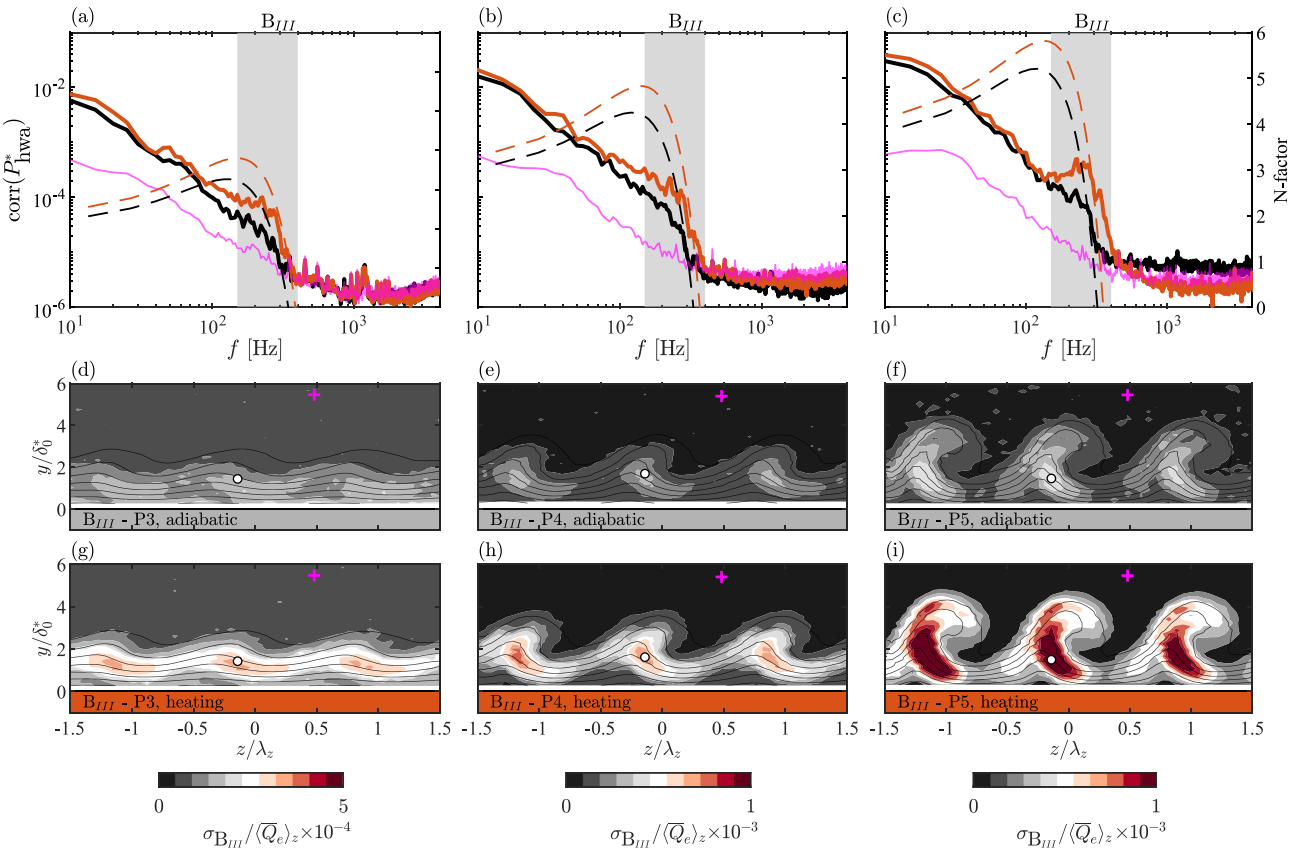

Fig. 8. (a–c) Non-dimensional spectra of corrected ($\mathrm{corr}(P^*_{\mathrm{hwa}})$, thick lines) HWA velocity fluctuations, extracted at the location marked by ∘ in the contours. Freestream PSD (+, magenta line) and CLPSE N-factor (dashed) results are also shown. The gray band indicates the spectral range B_{III} : 150 Hz ≤ f ≤ 400 Hz. (d–f) Contours of B_{III}-filtered velocity fluctuations in adiabatic (d–f) and wall-heating (g–i) conditions. Time-averaged flow is shown in black contour lines. All panels: results at plane P3 (a,d,g), P4 (b,e,h), and P5 (c,f,i).

5.2. Effect of wall-heating on T-CFI and type-III mode

Wall-heating also amplifies the T-CFI, as previously shown by both CLPSE and experimental results (see dashed lines in Fig. 7a,d and corrected bandpass-filtered velocity results in Fig. 7d,f). The destabilizing effect of wall heating on T-CFI has been previously reported by Ren and Kloker [13]. A higher amplitude of T-CFI and S-CFI can ultimately lead to stronger non-linear interaction and a subsequent amplification of type-III instabilities. To investigate the influence of wall heating on the development and growth of T-CFI and type-III mode, this section will analyze the spectral content and spatial topology of velocity fluctuations within the unstable T-CFI frequency band under both adiabatic and wall-heating conditions.

Fig. 8(a–c) present the PSD of the corrected HWA velocity fluctuations ($\mathrm{corr}(P^*_{\mathrm{hwa}})$) at planes P3, P4, and P5, respectively, extracted at locations of maximum spanwise shear (see circular markers in Fig. 8d–i). Superimposed dashed lines in the PSD curves (Fig. 8a–c) represent the N-factors for different T-CFI frequencies computed with CLPSE, under both adiabatic and wall-heating conditions.

At planes P3 and P4, comparison between PSD results in adiabatic and wall-heating conditions (Fig. 8a–b) reveals a persistent and significant increase in spectral energy under wall-heating within the frequency band where CLPSE predicts unstable T-CFI (80 Hz $\lesssim f \lesssim$ 400 Hz). Interestingly, at plane P5 (Fig. 8c), the energy increase due to wall-heating becomes most pronounced in a narrower frequency band, namely 150 Hz ≤ f ≤ 400 Hz, indicated by a shaded gray region in Fig. 8(a–c). The absence of a clear amplification at the lower-frequency T-CFI regime from plane P5 (Fig. 8c) may be attributed to differences in the flow's receptivity for distinct frequencies. The spectral results in Fig. 8(a–c) suggest that frequencies centered around $f \approx 250$ Hz might feature higher initial amplitudes at receptivity compared with lower frequencies. Consequently, although these frequencies exhibit smaller amplification rates (see N-factor curves in Fig. 8a–c), because of the higher initial amplitudes at receptivity, they ultimately reach higher amplitudes farther downstream.

Fig. 8(d–i) show bandpass-filtered velocity contours within the frequency band B_{III} : 150 Hz ≤ f ≤ 400 Hz, under both adiabatic and wall-heating conditions. All results were obtained by applying a bandpass filter to the corrected HWA signal. For details regarding the bandpass filtering procedure, refer to Section 2.3.

Across all planes (Fig. 8d–i), B_{III}-filtered contours exhibit a spatial organization characteristic of type-III secondary instability development, with strongest velocity fluctuations emerging at the inner side of the upwelling S-CF vortex, where the interaction between traveling and steady CFI becomes most important. As the T-CFI and S-CFI amplitudes increase, their enhanced interaction leads to the upward displacement of the T-CF vortices within low-momentum regions [41]. This upward lifting of the high-RMS region is progressively observed from planes P3 to P5 in Fig. 8(d–i). The spatial development and topology observed from Fig. 8(d–i) is concurrent with previous experimental observations of type-III instability development in S-CFI dominated transition scenarios, such as the forcing case [18|12] described by White and Saric [41].

Contours of B_{III}-filtered velocity fluctuations reveal consistently higher amplitudes under wall-heating than under adiabatic conditions (Fig. 8d–i). To effectively quantify their streamwise growth, B_{III}-filtered velocity fluctuations are integrated over the y–z planes to obtain a measure of their amplitude, $a_{B_{III}}$, as defined in Eq. (23). The streamwise evolution of $a_{B_{III}}$ for both thermal conditions is presented in Fig. 9(g). Two distinct stages can be identified: the linear growth of

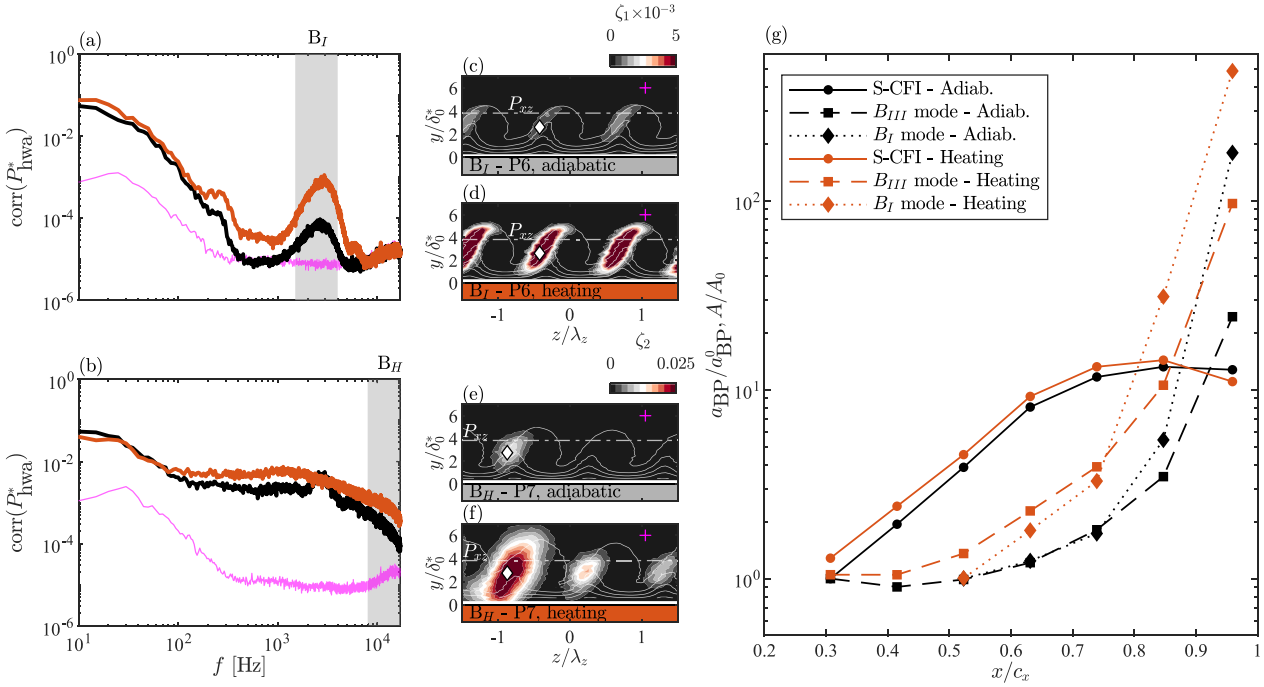

Fig. 9. (a–b) Non-dimensional spectra of corrected ($\mathrm{corr}(P^*_{\mathrm{hwa}})$, thick lines) HWA velocity fluctuations, extracted at the location marked by ⋄ in the contours at planes P6 (a) and P7 (b). Freestream PSD (+ in contours) is shown in magenta. Gray band indicates the spectral ranges B_I : 1.5 kHz ≤ f ≤ 4 kHz (a) and B_H : f ≥ 8 kHz (b). (c–d) Contours of B_I-filtered velocity fluctuations ($\zeta_1 = \sigma_{B_I}/\langle\overline{Q}_e\rangle_z$) in adiabatic (c) and wall-heating (d) conditions at plane P6. (e–f) Contours of B_H-filtered velocity fluctuations ($\zeta_2 = \sigma_{B_H}/\langle\overline{Q}_e\rangle_z$) in adiabatic (e) and wall-heating (f) conditions at plane P7. Time-averaged flow is shown in white contour lines. (e) Amplitude of S-CFI (A/A_0, ——∘) and bandpass-filtered velocity fluctuations ($a_{\mathrm{BP}}/a^0_{\mathrm{BP}}$, Eq. (23)) at B_{III} (- - -□) and B_I (·····⋄). Adiabatic amplitude values are used for normalization: $A_0/\langle\bar{Q}_e\rangle_z = 0.014$ (at plane P1), $a^0_{B_{III}}/\langle\bar{Q}_e\rangle_z = 9\times10^{-5}$ (at plane P1), and $a^0_{B_I}/\langle\bar{Q}_e\rangle_z = 4\times10^{-5}$ (at plane P3). All panels: adiabatic results in black and wall-heating in orange.

the T-CFI occurring approximately upstream of P4, and the subsequent nonlinear and more explosive amplification of the type-III mode downstream of P4. The composite nature of these low-frequency fluctuations explains the more gradual upstream growth behavior of $a_{B_{III}}$ compared to that of type-I (a_{B_I}) secondary instabilities.

Under wall-heating conditions, Fig. 9(g) shows that $a_{B_{III}}$ reaches amplitudes up to three times higher than those observed under adiabatic conditions. These observations further confirm the strong destabilizing influence of wall heating on both the T-CFI and the type-III mode.

5.3. Effect of wall-heating on type-I mode

Spectral analysis of HWA velocity fluctuations at downstream planes P6 and P7 (Fig. 9a,b) reveals the influence of wall-heating in regions of strong non-linear interactions right before laminar flow breakdown. These PSD signals are extracted at the outer side of the upwelling region, where type-I instabilities develop (note ⋄ marker in Fig. 9c-f). At plane P6 (Fig. 9a), the energy content within the high-frequency band (B_I, 1.5 kHz ≤ f ≤ 4 kHz), ascribed to type-I secondary instability development, appears 15 times higher with wall-heating compared to adiabatic conditions. At plane P7 (Fig. 9b), the flow presents a more advanced stage of laminar breakdown under wall-heating conditions compared to adiabatic conditions, as indicated by the more uniform distribution of spectral energy.

Fig. 9(c,d) show the B_I-filtered contours of velocity fluctuations (1.5 kHz ≤ f ≤ 4 kHz) at plane P6 under both adiabatic (Fig. 9c) and wall-heating (Fig. 9d) conditions. These high-frequency fluctuations, previously ascribed to type-I secondary instability development, are spatially organized along the upwelling side of the vortex, coinciding with regions of high spanwise shear (see Fig. 6f). This behavior is consistent with previous experimental (e.g., [56]) and numerical (e.g., [32]) studies. Contours of σ_{B_I} under wall-heating conditions (Fig. 9d) exhibit velocity fluctuations that are approximately twice as large as those observed under adiabatic conditions (Fig. 9c). The increased amplification of type-I secondary instabilities is primarily attributed to the stronger spanwise modulation induced by the higher-amplitude CF vortices in the boundary layer under wall-heating conditions (e.g., compare time-averaged velocity fields in Fig. 3c,g). The resulting increase of spanwise velocity shears enhances the growth of secondary instabilities (e.g., [41]).

Finally, Fig. 9(g) presents the streamwise evolution of the type-I secondary instability amplitude (a_{B_I}), computed as defined in Eq. (23). A rapid increase in amplitude is observed at the last two streamwise stations, between planes P6 and P7, consistent with the characteristic explosive growth of inflectional (KH-like) instabilities constituting the type-I mode [32]. Comparable trends have also been reported in experimental studies conducted under similar low free-stream turbulence intensities ($T_u \leq 0.1\%$, e.g., [41]).

5.4. Laminar flow breakdown under wall-heating conditions

Results presented in previous sections reveal significant amplification of both type-III and type-I secondary instabilities under wall-heating conditions. Specifically, at $x/c_x \approx 0.85$ (immediately upstream of laminar flow breakdown) the amplitude of type-III secondary instabilities ($a_{B_{III}}$, defined in Eq. (23)) is approximately 3 times greater than in adiabatic conditions. Similarly, the amplitude of type-I secondary instabilities is increased by a factor of 5.7.

Fig. 9(e,f) shows the spatial organization of highpass-filtered velocity fluctuations with a cut-off frequency at f = 8 kHz. This filtering effectively isolates turbulent fluctuations from those associated with secondary CF instabilities [58]. From these results, it can be observed that high-amplitude turbulent fluctuations originate at the upwelling

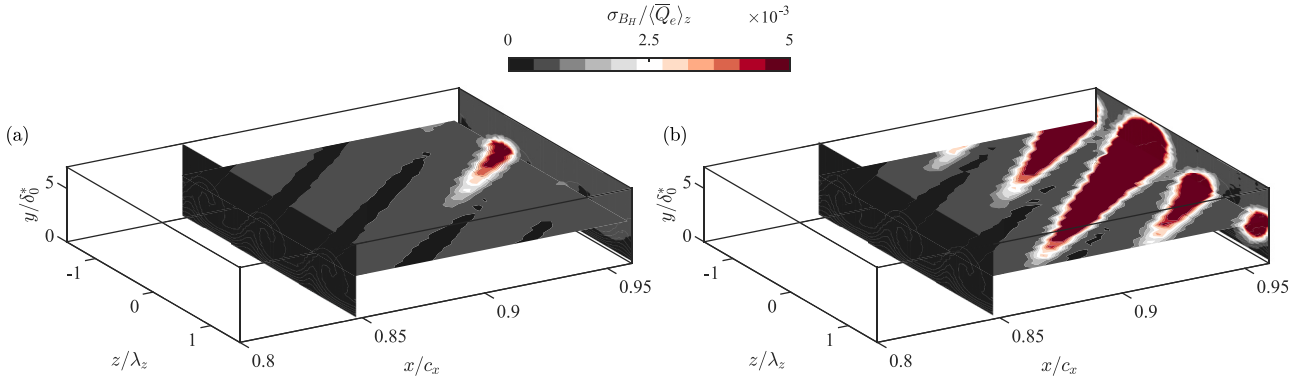

Fig. 10. Spatial evolution of highpass-filtered ($f \geq 8$ kHz, B_H) velocity fluctuations representing laminar flow breakdown. Results are presented at HWA yz planes P6 and P7, along with results at one xz plane extracted at $y/\delta_0^* \approx 4$, spanning the streamwise stations between P6 and P7. White contour lines in yz planes indicate the time-averaged flow ($\overline{Q}$). Results are shown in both adiabatic (a) and wall-heating (b) conditions. Note that the external velocity ($\langle\overline{Q}_e\rangle_z$) used to normalize σ_{B_H} corresponds to the one at plane P6.

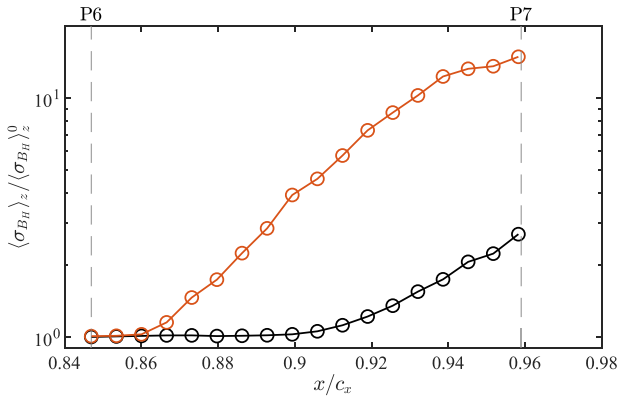

Fig. 11. Spanwise-averaged highpass-filtered ($f \geq 8$ kHz, B_H) velocity fluctuations at plane P_{xz} (see plane in Fig. 10). Adiabatic (——○) and wall-heating (——○) conditions are shown. Adiabatic amplitude values are used for normalization: $\langle\sigma_{B_H}/\overline{Q}_e\rangle_z^0 = 4.7 \times 10^{-4}$ (at plane P6).

side of the CF vortex (Fig. 9e,f), indicating that laminar flow breakdown is initiated by type-I secondary instabilities. Thus, despite the substantial amplification of type-III modes under wall-heating, the onset of laminar flow breakdown is still initiated by type-I secondary instabilities under both thermal conditions.

During these experiments, no dedicated experimental methods for laminar-to-turbulent detection, such as infrared thermography or temperature sensitive paint, were employed. Nevertheless, the advancement of laminar-to-turbulent transition can be qualitatively estimated by analyzing the streamwise evolution of high-frequency velocity fluctuations, representing the onset of turbulence. Similar to Fig. 9(e,f), Fig. 10 shows contours of highpass-filtered velocity fluctuations at B_H ($f \geq 8$ kHz) for the last two yz HWA planes (P6 and P7) and for a xz HWA plane acquired at $y/\delta_0^* \approx 4$ (white dashed line in Fig. 9f–g). The wall-normal location of plane P_{xz} is chosen based on the y-region where the type-I secondary instability reaches its maximum amplitude, i.e., where $\max(\langle\sigma_{B_I}\rangle_z)$.

Contours of σ_{B_H} at plane P_{xz} in Fig. 10 reveal an evident premature onset of turbulent wedges in the streamwise direction under wall-heating compared to adiabatic conditions. Spanwise averaging the high-frequency fluctuations ($\langle\sigma_{B_H}\rangle_z$) from plane P_{xz} provides insight into the streamwise growth of turbulent fluctuations, as shown in Fig. 11. From this figure, it is observed that turbulent fluctuations start to amplify at an earlier streamwise station ($x/c_x \approx 0.86$) compared to adiabatic conditions ($x/c_x \approx 0.9$). The premature onset of flow breakdown observed from experiments offers plausible evidence that wall heating also promotes a premature onset of laminar-to-turbulent transition.

6. Conclusions

The influence of wall heating on the development of the crossflow instability was investigated through experiments and stability simulations. The primary S-CF mode was conditioned using DREs placed at the leading edge of a 45° swept flat plate tested in a low-turbulence environment ($T_u \leq 0.05\%$) at a chord-based Reynolds number of $\mathrm{Re}_{c_X} = 8.56 \times 10^5$. The backside of the flat plate was equipped with an electric heater to achieve quasi-uniform wall heating, reaching a maximum wall temperature ratio of $T_w/T_e = 1.055$. HWA and CWA provided detailed velocity and temperature measurements, enabling characterization of the time-averaged flow and the steady and unsteady perturbation content under both adiabatic and wall-heating conditions. HWA scans at multiple streamwise locations enabled characterization of S-CFI evolution through the linear, nonlinear, and final transition stages. This comprehensive experimental dataset facilitated direct comparison with CNPSE results under both thermal conditions.

Upstream of $x/c_x \approx 0.5$, spanwise-and time-averaged velocity ($\langle\overline{Q}\rangle_z$) and temperature ($\langle\overline{T}\rangle_z$) profiles show good agreement with baseflow results from numerical boundary-layer theory. The perturbation field also shows close agreement with both linear and nonlinear PSE results in terms of HWA steady perturbation profiles ($\hat{q}_{rms}$) and S-CFI amplitude growth (A), confirming linear S-CFI amplification in this region. Both experimental and numerical results reveal that wall-heating leads to higher momentum deficit, while numerical results additionally show a larger crossflow component ($\overline{w}_i$). Combined, these lead to stronger S-CFI development under wall heating. This is evidenced in both experiments and PSE results, where the S-CFI amplitude undergoes an increase of ≈ 30% within this first linear regime (i.e. $x/c_x \leq 0.5$).

Downstream of $x/c_x \approx 0.5$, the experimentally measured velocity and temperature profiles start to deviate from baseflow results. Nevertheless, good agreement is observed when the meanflow Distortion (MFD) predicted from CNPSE is added to the numerical baseflow. These observations are consistent with previous studies (e.g. [43]), namely that beyond this point, only nonlinear PSE computations are able to accurately resolve the S-CFI development captured by the experiments.

Both HWA measurements and CNPSE results reveal that wall-heating promotes an earlier onset of non-linear interactions, as evidenced by the larger amplitudes of both higher S-CF harmonics and MFD. Interestingly, despite both thermal cases experiencing the same free-stream turbulence intensity, S-CFI saturation occurs at a higher amplitude under wall heating ($A/\langle\bar{Q}_e\rangle_z = 0.175$) compared to adiabatic

conditions ($A/\langle\bar{Q}_e\rangle_z = 0.159$). This suggests that wall heating increases the total energy within the boundary layer, enabling the perturbation field to sustain higher energy levels before laminar breakdown, as reflected by the larger saturation amplitude.

Spectral analysis of the HWA signal reveals a significant increase in spectral energy under wall-heating, with two distinct frequency bands being particularly affected. The first band, corresponding to the low-frequency range (B_{III} : 150 Hz $\leq f \leq$ 400 Hz), is associated with T-CFI and type-III instabilities.

Due to the strong destabilizing effect of wall-heating on T-CFI (e.g. [13]), the amplification of velocity fluctuations within this spectral band is evident already during the linear growth regime, where the amplitude of these low-frequency fluctuations ($a_{B_{III}}$, Eq. (23)) is already twice as high with wall-heating. Further downstream, nonlinear interactions between S-CFI and T-CFI trigger type-III instabilities, leading to a steeper streamwise amplification near laminar flow breakdown, with $a_{B_{III}}$ reaching levels three times higher under wall-heating.

The second spectral band showing significant amplification of velocity fluctuations under wall-heating corresponds to the higher-frequency range (B_I : 1.5 kHz $\leq f \leq$ 4 kHz), associated with type-I instabilities. Due to their characteristic explosive growth, the amplitude of these high-frequency fluctuations (a_{B_I}, Eq. (20)) reaches values five times higher under wall-heating before laminar flow breakdown. Finally, high-pass filtered velocity fluctuations at $f \simeq 8$ kHz reveal an earlier onset of turbulent fluctuations with wall-heating, suggesting a potentially premature laminar-to-turbulent transition.

To the best of the authors' knowledge, this work provides the first experimental evidence quantifying the effect of wall-heating on the transition process of crossflow vortices. The analysis covers its impact on the time-averaged flow as well as on the growth of steady and unsteady perturbation fields across both linear and nonlinear regimes. A key finding of this study is the strong destabilizing effect of wall-heating on T-CFI and type-III instabilities, demonstrated experimentally for the first time in this work. In light of these observations, one plausible interpretation is that, at sufficiently higher wall-temperature ratios (T_w/T_e), T-CFI amplitudes may become comparable to (or even exceed) those of S-CFI. In that case, T-CFI could dominate the transition process, potentially leading to scenarios that more closely resemble those observed in higher-T_u environments (e.g., $T_u = 0.19\%$ case in [21]). Future research is needed to understand the transition behavior at higher wall-temperature ratios, where T-CFI may dominate transition despite the low T_u levels typical of flight conditions.

Collectively, the findings presented in this work demonstrate that even moderate wall-heating ratios can substantially affect swept-wing boundary-layer transition. More specifically, heating the surface to a local maximum of $T_w/T_e \approx 1.055$ (Fig. 2b) caused the onset of turbulence fluctuations to occur $\Delta x/c_x \approx 4\%$ upstream. From a practical perspective, these results lead to two important conclusions: first, they highlight the potential of wall-cooling as a viable flow-control strategy to delay laminar–turbulent transition; second, they indicate that, if OML cooling is to be integrated in future electric commercial aircraft, wall-to-freestream temperature ratios must be carefully monitored and controlled to avoid compromising aerodynamic efficiency. However, a full quantitative assessment of the impact of wall heating on OML cooling can only be achieved through experiments at higher Reynolds and Mach numbers representative of transport aircraft in cruise.

CRediT authorship contribution statement

Marina Barahona: Writing – review & editing, Writing – original draft, Project administration, Methodology, Investigation, Data curation, Conceptualization. **Yifu Chen:** Writing – review & editing, Methodology, Investigation, Conceptualization. **Alberto F. Rius-Vidales:** Writing – review & editing, Investigation, Conceptualization. **Marios Kotsonis:** Writing – review & editing, Supervision, Investigation, Funding acquisition, Conceptualization.

Declaration of competing interest

The authors declare that they have no known competing financial interests or personal relationships that could have appeared to influence the work reported in this paper.

Acknowledgments

The authors would like to acknowledge the support and funding provided by the Department of Flow Physics and Technology at TU Delft and the European Research Council (grant number 803082) for this research project. Special recognition is extended to Tim van de Weijer for his significant contributions to the design and development of the experiments, and to Dr. Woutijn Baars, for his valuable insights and constructive supervision. The authors also express their sincere gratitude to Dr. Jie Ren and Dr. Markus Kloker for generously sharing their numerical data, which was essential for verifying the numerical tools presented in this work. Further thanks are due to Dr. Marco Costantini for his ongoing scientific counsel and endless interest in the project, and to Dr. Ramis Örlü for his valuable input on cold wires. Additionally, the authors appreciate the technical contributions of Stefan Bernardy, Emiel Langedijk, and Pieter Duyndham during the experiments. Special mention also goes to Sven Westerbeek and Jordi Casacuberta for their insightful input and assistance in developing the numerical framework.

Data availability

Data will be made available on request.

References

[1] H. Kellermann, M. Lüdemann, M. Pohl, M. Hornung, Design and optimization of ram air–based thermal management systems for hybrid-electric aircraft, Aerospace 8 (1) (2020) http://dx.doi.org/10.3390/aerospace8010003.

[2] C.K. Sain, J. Hänsel, S. Kazula, Conceptual design of air and thermal management in a nacelle-integrated fuel cell system for an electric regional aircraft, in: AIAA AVIATION 2023 Forum, 2023, p. 3875, http://dx.doi.org/10.2514/6.2023-3875.

[3] F. Barbir, T. Gómez, Efficiency and economics of proton exchange membrane (PEM) fuel cells, Int. J. Hydrog. Energy 22 (10) (1997) 1027–1037, http://dx.doi.org/10.1016/S0360-3199(96)00175-9.

[4] E. Sozer, D. Maldonado, K. Bhamidipati, S.L. Schnulo, Computational evaluation of an OML-based heat exchanger concept for heather, in: 2020 AIAA/IEEE Electric Aircraft Technologies Symposium, EATS, IEEE, 2020, pp. 1–22.

[5] M. Coutinho, D. Bento, A. Souza, R. Cruz, F. Afonso, F. Lau, A. Suleman, F.R. Barbosa, R. Gandolfi, W.A. Junior, et al., A review on the recent developments in thermal management systems for hybrid-electric aircraft, Appl. Therm. Eng. 227 (2023) 120427, http://dx.doi.org/10.1016/j.applthermaleng.2023.120427.

[6] R.D. Joslin, Aircraft laminar flow control, Annu. Rev. Fluid Mech. (1998) 1–29, http://dx.doi.org/10.1146/annurev.fluid.30.1.1.

[7] Y.S. Kachanov, V.V. Kozlov, V.Y. Levchenko, Experimental study of the influence of cooling on the stability of laminar boundary layers, in: Izvestia Sibirskiogo Otdielenia Ak. Nauk SSSR, in: Seria Technicheskikh Nauk, 1974.

[8] M. Costantini, S. Risius, C. Klein, Surface temperature effects on boundary-layer transition at various subsonic Mach numbers and streamwise pressure gradients, in: New Results in Numerical and Experimental Fluid Mechanics XII, Springer International Publishing, 2020, pp. 155–164, http://dx.doi.org/10.1007/978-3-030-25253-3_15.

[9] L.I. Boehman, M.G. Mariscalco, Stability of Highly-Cooled Compressible Laminar Boundary Layers, Technical Report TR-76-148, U.S. Air Force Flight Dynamics Laboratory, Ohio, 1976.

[10] L.M. Mack, Boundary Layer Stability Theory: An AGARD Special Course on Stability and Transition of Laminar Flow, Technical Report 709, AGARD, 1984.

[11] L.M. Mack, On the stabilization of three-dimensional boundary layers by suction and cooling, in: Laminar–Turbulent Transition, Springer, 1980, pp. 223–238.

[12] S.G. Lekoudis, Stability of the boundary layer on a swept wing with wall cooling, AIAA J. 18 (9) (1980) 1029–1035, http://dx.doi.org/10.2514/3.50852.

[13] J. Ren, M. Kloker, Instabilities in three-dimensional boundary-layer flows with a highly non-ideal fluid, J. Fluid Mech. 951 (2022) A9, http://dx.doi.org/10.1017/jfm.2022.845.

[14] F.P. Bertolotti, H. Bieler, Stability analysis of two- and three-dimensional boundary layer flows with varied wall temperatures, in: New Results in Numerical and Experimental Fluid Mechanics: Contributions to the 10th AG STAB/DGLR Symposium Braunschweig, Germany 1996, 1997, pp. 64–70, http://dx.doi.org/10.1007/978-3-322-86573-1_8.
[15] J. Lemarechal, M. Costantini, C. Klein, M.J. Kloker, W. Würz, H.B. Kurz, T. Streit, S. Schaber, Investigation of stationary-crossflow-instability induced transition with the temperature-sensitive paint method, Exp. Therm. Fluid Sci. 109 (2019) 109848, http://dx.doi.org/10.1016/j.expthermflusci.2019.109848.
[16] W. Saric, H. Reed, Toward practical laminar flow control-remaining challenges, in: 2nd AIAA Flow Control Conference, 2004, p. 2311, http://dx.doi.org/10.2514/6.2004-2311.
[17] E. White, W. Saric, R. Gladden, P. Gabet, Stages of swept-wing transition, in: 39th Aerospace Sciences Meeting and Exhibit, 2001, p. 271, http://dx.doi.org/10.2514/6.2001-271.
[18] R.S. Downs, E.B. White, Free-stream turbulence and the development of crossflow disturbances, J. Fluid Mech. 735 (2013) 347–380, http://dx.doi.org/10.1017/jfm.2013.484.
[19] J. Eppink, R. Wlezien, Data analysis for the NASA/Boeing hybrid laminar flow control crossflow experiment, in: 41st AIAA Fluid Dynamics Conference and Exhibit, 2011, p. 3879, http://dx.doi.org/10.2514/6.2011-3879.
[20] R. Merino-Martínez, A.R. Carpio, L.T.L. Pereira, S. van Herk, F. Avallone, D. Ragni, M. Kotsonis, Aeroacoustic design and characterization of the 3D-printed, open-jet, anechoic wind tunnel of Delft University of Technology, Appl. Acoust. 170 (2020) 107504, http://dx.doi.org/10.1016/j.apacoust.2020.107504.
[21] R.S. Downs, Environmental Influences on Crossflow Instability (Ph.D. thesis), Texas A&M University, 2012.
[22] A.F. Rius-Vidales, M. Barahona, M. Kotsonis, Swept transition experimental platform (STEP), in: AIAA Scitech 2024 Forum, 2024, p. 0942, http://dx.doi.org/10.2514/6.2024-0942.
[23] M.W. Tufts, H.L. Reed, B.K. Crawford, G.T. Duncan, W.S. Saric, Computational investigation of step excrescence sensitivity in a swept-wing boundary layer, J. Aircr. 54 (2) (2017) 602–626, http://dx.doi.org/10.2514/1.C033892.
[24] A.F. Rius-Vidales, M. Kotsonis, Influence of a forward-facing step surface irregularity on swept wing transition, AIAA J. 58 (12) (2020) 5243–5253, http://dx.doi.org/10.2514/1.J059566.
[25] H. Deyhle, H. Bippes, Disturbance growth in an unstable three-dimensional boundary layer and its dependence on environmental conditions, J. Fluid Mech. 316 (1996) 73–113, http://dx.doi.org/10.1017/S0022112096000456.
[26] W. Saric, R. Carrillo, M. Reibert, Leading-edge roughness as a transition control mechanism, in: 36th AIAA Aerospace Sciences Meeting and Exhibit, 1998, p. 781, http://dx.doi.org/10.2514/6.1998-781.
[27] G. Zoppini, S. Westerbeek, D. Ragni, M. Kotsonis, Receptivity of crossflow instability to discrete roughness amplitude and location, J. Fluid Mech. 939 (2022) A33, http://dx.doi.org/10.1017/jfm.2022.220.
[28] R.H. Radeztsky, M.S. Reibert, W.S. Saric, Effect of isolated micron-sized roughness on transition in swept-wing flows, AIAA J. 37 (11) (1999) 1370–1377, http://dx.doi.org/10.2514/2.635.
[29] D. Tempelmann, L.U. Schrader, A. Hanifi, L. Brandt, D.S. Henningson, Swept wing boundary-layer receptivity to localized surface roughness, J. Fluid Mech. 711 (2012) 516–544, http://dx.doi.org/10.1017/jfm.2012.405.
[30] R. Örlü, R. Vinuesa, Thermal anemometry, in: Experimental Aerodynamics, CRC Press, Taylor & Francis Group, 2017, pp. 257–303, http://dx.doi.org/10.1201/9781315371733-12.
[31] M. Hultmark, A.J. Smits, Temperature corrections for constant temperature and constant current hot-wire anemometers, Meas. Sci. Technol. 21 (10) (2010) 105404, http://dx.doi.org/10.1088/0957-0233/21/10/105404.
[32] P. Wassermann, M. Kloker, Mechanisms and passive control of crossflow-vortex-induced transition in a three-dimensional boundary layer, J. Fluid Mech. 456 (2002) 49–84, http://dx.doi.org/10.1017/S0022112001007418.
[33] E.B. White, F.G. Ergin, Using laminar-flow velocity profiles to locate the wall behind roughness elements, Exp. Fluids 36 (2004) 805–812, http://dx.doi.org/10.1007/s00348-003-0766-y.
[34] Z. Liu, Compressible Falkner–Skan–Cooke boundary layer on a flat plate, Phys. Fluids 33 (2021) http://dx.doi.org/10.1063/5.0075233.
[35] J. Casacuberta, S. Hickel, S. Westerbeek, M. Kotsonis, Direct numerical simulation of interaction between a stationary crossflow instability and forward-facing steps, J. Fluid Mech. 943 (2022) A46, http://dx.doi.org/10.1017/jfm.2022.456.
[36] T. Herbert, Parabolized stability equations, Annu. Rev. Fluid Mech. 29 (1997) 245–283, http://dx.doi.org/10.1146/annurev.fluid.29.1.245.
[37] S. Westerbeek, Development of a Nonlinear Parabolized Stability Equation (NPSE) Analysis Tool for Spanwise Invariant Boundary Layers (Master's Thesis), TU Delft, 2020.
[38] S. Westerbeek, S. Hulshoff, H. Schuttelaars, M. Kotsonis, DeHNSSo: The delft harmonic Navier-Stokes solver for nonlinear stability problems with complex geometric features, Comput. Phys. Comm. 302 (2024) 109250, http://dx.doi.org/10.1016/j.cpc.2024.109250.
[39] N.B. Oliviero, EPIC: A New and Advanced Nonlinear Parabolized Stability Equation Solver (Ph.D. thesis), Texas A and M University, 2015.
[40] F. Li, M.M. Choudhari, L. Duan, Direct numerical simulation of transition due to traveling crossflow vortices, in: 45th AIAA Fluid Dynamics Conference, American Institute of Aeronautics and Astronautics, Dallas, TX, 2015, http://dx.doi.org/10.2514/6.2015-2771.
[41] E.B. White, W.S. Saric, Secondary instability of crossflow vortices, J. Fluid Mech. 525 (2005) 275–308, http://dx.doi.org/10.1017/S002211200400268X.
[42] J. Serpieri, M. Kotsonis, Three-dimensional organisation of primary and secondary crossflow instability, J. Fluid Mech. 799 (2016) 200–245, http://dx.doi.org/10.1017/jfm.2016.379.
[43] T.S. Haynes, H.L. Reed, Simulation of swept-wing vortices using nonlinear parabolized stability equations, J. Fluid Mech. 405 (2000) 325–349, http://dx.doi.org/10.1017/S0022112099007260.
[44] P. Welch, The use of fast Fourier transform for the estimation of power spectra: A method based on time averaging over short, modified periodograms, IEEE Trans. Audio Electroacoust. 15 (2) (1967) 70–73, http://dx.doi.org/10.1109/TAU.1967.1161901.
[45] R.J. Adrian, P. Moin, Stochastic estimation of organized turbulent structure: homogeneous shear flow, J. Fluid Mech. 190 (1988) 531–559, http://dx.doi.org/10.1017/S0022112088001442.
[46] W.J. Baars, N. Hutchins, I. Marusic, Spectral stochastic estimation of high-Reynolds-number wall-bounded turbulence for a refined inner-outer interaction model, Phys. Rev. Fluids 1 (2016) 054406, http://dx.doi.org/10.1103/PhysRevFluids.1.054406.
[47] C.E. Tinney, F. Coiffet, J. Delville, A.M. Hall, P. Jordan, M.N. Glauser, On spectral linear stochastic estimation, Exp. Fluids 41 (2006) 763–775, http://dx.doi.org/10.1007/s00348-006-0199-5.
[48] A.V. Oppenheim, R.W. Schafer, Discrete-Time Signal Processing, third ed., Pearson, Upper Saddle River, NJ, USA, 2010.
[49] G. Bonfigli, M. Kloker, Secondary instability of crossflow vortices: validation of the stability theory by direct numerical simulation, J. Fluid Mech. 583 (2007) 229–272, http://dx.doi.org/10.1017/S0022112007006179.
[50] H. Bippes, Basic experiments on transition in three-dimensional boundary layers dominated by crossflow instability, Prog. Aerosp. Sci. 35 (4) (1999) 363–412, http://dx.doi.org/10.1016/S0376-0421(99)00002-0.
[51] M.S. Reibert, W.S. Saric, R.B. Carrillo, K.L. Chapman, Experiments in nonlinear saturation of stationary crossflow vortices in a swept-wing boundary layer, in: 34th Aerospace Sciences Meeting and Exhibit, 1996, p. 184, http://dx.doi.org/10.2514/6.1996-184.
[52] W.S. Saric, R.B. Carrillo, M.S. Reibert, Nonlinear stability and transition in 3-D boundary layers, Meccanica 33 (1998) 469–487, http://dx.doi.org/10.1023/A:1004368526215.
[53] M.R. Malik, F. Li, C.L. Chang, Crossflow disturbances in three-dimensional boundary layers: nonlinear development, wave interaction and secondary instability, J. Fluid Mech. 268 (1994) 1–36, http://dx.doi.org/10.1017/S0022112094001242.
[54] S. Hein, Linear and nonlinear growth of secondary instabilities of stationary crossflow vortices studied by parabolized stability equations, in: New Results in Numerical and Experimental Fluid Mechanics XI, Springer International Publishing, 2017, pp. 219–228, http://dx.doi.org/10.1007/978-3-319-64519-3_20.
[55] W. Koch, F.P. Bertolotti, A. Stolte, S. Hein, Nonlinear equilibrium solutions in a three-dimensional boundary layer and their secondary instability, J. Fluid Mech. 406 (2000) 131–174, http://dx.doi.org/10.1017/S0022112099007387.
[56] M.R. Malik, F. Li, M.M. Choudhari, C. Chang, Secondary instability of crossflow vortices and swept-wing boundary-layer transition, J. Fluid Mech. 399 (1999) 85–115, http://dx.doi.org/10.1017/S0022112099006291.
[57] J.S. Bendat, A.G. Piersol, Random Data: Analysis and Measurement Procedures, John Wiley & Sons, 2011, http://dx.doi.org/10.1002/9781118032428.
[58] A.F. Rius-Vidales, M. Kotsonis, Unsteady interaction of crossflow instability with a forward-facing step, J. Fluid Mech. 939 (2022) A19, http://dx.doi.org/10.1017/jfm.2022.151.